Spring 2017

Structural Evolution of the San Juan Thrust System, Orcas and Shaw Islands, WA

Kevin Quillan
Western Washington University, quillak@wwu.edu

STRUCTURAL EVOLUTION OF THE SAN JUAN THRUST SYSTEM, ORCAS AND SHAW ISLANDS, WA

By

Kevin Quillan

Accepted in Partial Completion
Of the Requirements for the Degree
Master of Science

Kathleen L. Kitto, Dean of the Graduate School

ADVISORY COMMITTEE

Chair, Dr. Elizabeth Schermer

Dr. Pete Stelling

Dr. Sean Mulcahy

Master's Thesis

In presenting this thesis in partial fulfillment of the requirements for a master's degree at Western Washington University, I grant Western Washington University the non-exclusive royalty-free right to archive, reproduce, distribute, and display the thesis in any form and all forms, including electronic format, via any digital library mechanisms maintained by WWU.

I represent and warrant this is my original work, and does not infringe or violate any rights of others. I warrant that I have obtained written permission from the owner of any third party copyrighted material included in these files.

I acknowledge that I retain ownership rights to the copyright of this work, including but not limited to the right to use all or part of this work in future works, such as articles or books.

Library users are granted permission for individual, research and non-commercial reproduction of this work for educational purposes only. Any further digital posting of this document requires specific permission from the author.

Any copying or publication of this thesis for commercial purposes, or for financial gain, is not allowed without my written permission.

Signature: _____Kevin Quillan_____

Date:_____5/19/2017_____

STRUCTURAL EVOLUTION OF THE SAN JUAN THRUST SYSTEM, ORCAS AND SHAW ISLANDS, WA

A Thesis
Presented to
The Faculty of
Western Washington University

In Partial Fulfillment
Of the Requirements for the Degree
Master of Sciences

By
Kevin Quillan
May 2017

ABSTRACT

The San Juan Thrust System represents the western elements of the Cascades orogen and preserves evidence for Cretaceous Cordilleran margin tectonics. The kinematics of deformation phases and their temporal relationship to accretionary wedge high-pressure low-temperature metamorphism remains uncertain. The structural and metamorphic evolution of the San Juan Thrust System was studied on Orcas and Shaw Islands in Western Washington. Detailed field mapping indicates that a widespread S1 flattening fabric (formed during D1) is subparallel to and cut by an S2 fabric found within brittle-ductile shear zones that bound the terranes (formed during D2). Post-cleavage brittle structures (formed during D3) offset terrane contacts and S2 fabrics and include cm- to m-scale slip on normal, strike-slip, and thrust faults that have mutual crosscutting relationships. Metamorphic investigations utilizing vein mineralogy and fluid inclusion analysis reveal the pressure and temperature relations during each stage of deformation. Maximum temperatures of ~200˚C and pressures of ≥5.5 kbar are indicated by both the preservation of aragonite within D1-D3 veins, and by a minor crystal-plastic component of quartz deformation within D2 shear zones. These conditions are interpreted to indicate deformation occurred in an accretionary wedge setting.

Using pressure-temperature constraints and kinematics of each event, I suggest a tectonic model that includes (1) D1 terrane accretion and fabric formation somewhere south along the continental margin, (2) NW-directed translation along the margin during oblique subduction as terranes were assembled on top of one another into their current nappe stack along D2 shear zones, and (3) subhorizontal extension and vertical thinning along brittle D3 structures. A predominance of margin-parallel extension in the forearc during D3 may be a response to “unbuttressed” collapse of an overthickened wedge, or from continued oblique subduction in the presence of a curved margin. This model supports previous interpretations of a NW-dominated thrust system, but high-pressure low-temperature constraints indicate that assembly of the nappe stack and later D3 brittle deformation represent continued structural evolution within an accretionary wedge. Results of this study indicate that the structures accountable for exhumation of the San Juan Thrust System and emplacement of terranes above the unmetamorphosed Wrangellia terrane are yet to be discovered.

Acknowledgements

Field and analytical work for this project have been supported by grants from the Geological Society of America, the Peter Misch Metamorphic Memorial Fellowship, and both the Geology Department and Research and Sponsored Programs at Western Washington University. Presentation of this research at the 2016 annual Geological Society of America conference was made possible by a travel grant received from the WWU Geology Department. I am indebted to my committee members Elizabeth Schermer, Pete Stelling, and Sean Mulcahy for their crucial guidance and feedback throughout my entire project. Brian Rusk is thanked for additional discussions regarding the applicability of the fluid inclusion results. Mike Craft provided useful suggestions regarding the analysis of XRD patterns. Kenneth Frank graciously provided structural data from Shaw Island. Field assistance from Kenneth Frank, Kylie Esselström, and Matt Howey was invaluable for data and sample collection during the 2015 summer field season. Joseph and Connie Jones were incredibly generous for providing housing during the rainy late summer months on Orcas Island. Indralaya Camp is thanked for allowing access to their useful shoreline outcrops during their busy summer season. Ben Paulson of the WWU Geology Department was always available for help while using the equipment available on campus. Lastly, I want to thank John Gillaspy and Ned Brown for useful discussions regarding the complicated nature of the SJTS rocks.

Table of Contents

List of Tables and Figures

Chapter 1

INTRODUCTION

The structural and metamorphic history of accreted terranes is important for understanding growth along continental margins during orogenic events. The kinematics of structures found within terranes and along their contacts are used to develop tectonic models for accretion along a continental margin. The San Juan Thrust System (SJTS), located in western Washington State, contains an assemblage of thrust-bounded terranes that are important for understanding the mid-Cretaceous tectonic development of the Pacific Northwest. The SJTS terranes contain a high-pressure low-temperature metamorphic signature (Glassely et al. 1976; Brandon et al., 1988; Maekawa and Brown, 1991), and previous workers (Brandon et al., 1988; Feehan and Brandon, 1999; Bergh, 2002) interpret that at least some of the deformation has occurred in an accretionary wedge. Three main kinematic models have been proposed; (1) SW-directed thrusting (Misch, 1966, Brandon et al., 1988, 1994; McGroder, 1991), (2), NW-directed thrusting (e.g., Brown, 1987; Maekawa and Brown, 1991), and (3) a two-stage model involving SW-directed thrusting followed by strike-slip faulting and NW-directed thrusting (Bergh, 2002). An attempt to reconcile the various SJTS models must include a comprehensive analysis of all the faults and fabrics as well as the metamorphic conditions during deformation.

Exhumed accretionary wedges provide the opportunity to examine deformation related to the accretion process (e.g., Meneghini et al., 2009). High-pressure low-temperature (HP-LT) minerals aragonite, prehnite, and lawsonite have been recorded in structures of the SJTS, suggesting an accretionary wedge setting during at least some of the deformation (Brandon et al., 1988; Glassely et al. 1976; Maekawa and Brown, 1991). Both brittle and ductile

structures are present in HP-LT accretionary wedge environments, and controls on deformation styles include temperature, depth, fluid pressure, and strain rates (e.g., Davis et al., 1983; Davis, 1996). Metamorphic constraints on deformation in the SJTS can be used to determine the relationship between depth and the other controls on structural evolution within an accretionary wedge.

The goal of this study is to investigate the kinematics and relative timing of structures along the well-exposed coastal outcrops of major terrane-bounding thrust faults on Orcas and Shaw Islands, Washington. Mineralogical, microstructural, and fluid inclusion constraints on pressure and temperature (P-T) conditions during each deformation event are used to interpret the evolution of terranes during and after deformation in an accretionary wedge setting. The new structural and metamorphic results are compared to previously proposed models of the SJTS.

GEOLOGIC SETTING

The SJTS represents the westernmost elements of the Northwest Cascades system (NWCS) and developed along the Mesozoic Cordilleran convergent margin (Fig. 1; Brandon and Cowan, 1985; Brown, 1987; Brandon et al., 1988; Whitney and McGroder, 1989; Rubin et al., 1990; Maekawa and Brown, 1991; McGroder, 1991; Brown et al., 2010; Brown, 2012). The thrust system is bounded to the north and west by the Wrangellia terrane and the Coast Plutonic Complex-Coast Mountain orogen (Fig. 1). The SJTS contains six Paleozoic to Mesozoic ocean floor and island arc-derived terranes (Danner, 1966; Monger and Ross, 1971; Brandon et al., 1988; Brown, 2012) that are now assembled in a SE-dipping stack of

four major nappes (Fig. 1; Brown, 2012). The Orcas thrust separates the Paleozoic Turtleback Complex and East Sound Group from the overlying Permian Deadman Bay terrane containing Deadman Bay volcanics and Orcas Chert ribbon chert (Brandon et al., 1988). The Rosario thrust contains fault slices of the Permian-Triassic Garrison Schist terrane, and separates Orcas Chert from the overlying Late Jurassic Constitution terrane (Brandon et al., 1988). The Lopez Structural Complex (LSC) separates Constitution terrane from the overlying Late Jurassic Fidalgo ophiolite (Brandon et al., 1988). The SJTS thrusts typically have a younger-on-older sequence. The unnamed thrust emplacing the Turtleback Complex over the East Sound Group on Orcas Island (Figs. 1, 2) is one of the few older-on-younger contacts. Evidence suggesting that the SJTS thrusts are major tectonic boundaries include 1) the presence of cataclasis along terrane boundaries and 2) slices of "exotic" Permian aged blueschist (Garrison Schist) faulted into the Rosario fault zone that suggests large displacements along terrane-bounding structures (Cowan and Miller, 1981; Brandon et al., 1988). Cowan and Brandon (1994) suggest a minimum of 30 km of slip along the Rosario thrust and the LSC alone in order to accommodate for the observed structural overlap of the terranes.

Timing constraints for thrusting and metamorphism are determined from isotopic Ar/Ar ages, fossil records, and detrital zircon ages. The age of thrusting is broadly constrained by late Aptian foraminifera (115-112 Ma) faulted into the LSC, and by clasts of SJTS debris within the overlying Nanaimo Group containing 84 Ma fossils (Ward, 1978; Brandon et al., 1988; Brown et al., 2005). Brown (2012) further constrains the ages of faulting based on a correlation between the SJTS and NWCS (Brown, 1987). Turonian

fossils and detrital zircon ages bracket the emplacement of Turtleback terrane over Wrangellia from <114 to >93 Ma (Brown and Gehrels, 2007; Brown, 2012). Individual thrusts are not dated in the SJTS, but Brown (2012) used a combination of detrital zircons and fossil ages from the NWCS to bracket nappe emplacement as a younging-upward sequence, with the Orcas nappe being emplaced at 110-88 Ma and the LSC faulting being post-112 Ma. Metamorphic ages are difficult to determine because the low-grade rocks contain little to no white mica. A phengite $^{40}Ar/^{39}Ar$ age of blueschist-facies meta-volcanic rock in the LSC constrains the age of metamorphism for rocks in this complex to ~124 ± 1 Ma (Brown et al., 2005).

The three main tectonic models proposed for the SJTS suggest different thrust system settings and contrasting kinematics (Table 1). The SW-directed thrust model interprets terranes thrust in a convergent zone between North America and the approaching Wrangellia (Misch, 1966; Brandon and Cowan, 1985; Brandon et al., 1988; McGroder, 1991; Cowan and Brandon, 1994). In the NW-directed thrust model, terranes were accreted or deposited somewhere south along the margin before being moved coastwise and thrust into a reentrant formed by the already accreted Wrangellia and Coast Plutonic Complex (Brown, 1987, 2012; Maekawa and Brown, 1991; Friedman and Armstrong, 1995). The two-stage model suggests SW-directed thrusting of terranes along the margin before partitioned orogen-parallel strike-slip faulting and NW-directed thrusting (Bergh, 2002). These tectonic models interpret that thrusting and HP-LT metamorphism took place in either an accretionary wedge setting (Brandon et al., 1988; Feehan and Brandon, 1999; Bergh, 2002; Schermer et al., 2007), in an

on-land thrust system (Brandon et al., 1988), or during obduction over Wrangellia (Maekawa and Brown, 1991; Brown, 2012).

METHODS

Structural investigation involved detailed outcrop description and mapping, kinematic analysis of faults, and microstructural analysis of fault rock. Maps by Brandon et al. (1988) and Vance (1975) were used to identify the locations of terrane contacts along coastal exposures (Figs. 1, 2, and Appendix). Faults and fabrics were measured and described at each locality, and cross-cutting relations were established. Samples of fault rock within brittle-ductile shear zones were collected for petrographic and microstructural analysis. Structures were plotted on equal area, lower-hemisphere stereonet projections using StereoWin v. 9.5.0. Kinematics were analyzed with FaultKinWin v. 7.4.1 (Allmendinger, 2016) using fault orientation, lineation, and slip sense data.

Sense of shear within shear zones and along faults was determined using outcrop- and microscopic-scale shear sense indicators. The sense of shear in shear zones was determined using S/C and Riedel fabrics (Berthe et al., 1979, Dresan, 1991), asymmetric porphyroclasts, folds, and slickenlines (Petit, 1987) and on faults using fault-propagation folds, chatter marks (Petit, 1987), en echelon extension veins (Shainin, 1950), slickenlines (Doblas, 1998), and shear veins (Durney and Ramsay, 1973). Microscopic-scale shear sense indicators in shear zones include S-C fabric geometries (Berthe et al., 1979), intrafolial folds of D1 foliation and veins, and sigmoid-shaped chlorite and wall rock porphyroclasts.

Veins were sampled to investigate mineralogy and to conduct fluid inclusion analysis. Samples were collected from structures with known kinematics and clear crosscutting

relationships. Twenty-three veins were analyzed using X-ray diffraction (XRD) for the presence of aragonite, lawsonite, and prehnite. Vein minerals were separated from the surrounding wall rock before being powdered to avoid sampling minerals not involved with vein formation. Samples were analyzed using a Rigaku Geigerflex X-ray diffractometer at Western Washington University and diffraction patterns were interpreted using JCPDS (1980) powder diffraction files. Forty-two samples were investigated for fluid inclusion analysis; detailed methodology, results, and discussion are presented in Chapter 2.

DESCRIPTIONS OF STRUCTURES

Structures on Orcas and Shaw Islands provide evidence of at least three different deformation events related to the SJTS (Table 1). Structures were tentatively grouped in the field using crosscutting relationships, deformation style, orientation, sense of slip, and apparent amount of strain accommodated along faults as evident by the amount cataclasite and/or fault zone width. Each deformation event is defined progressively as D1, D2, and D3 (Table 1). D1 and D2 structures include penetrative fabrics and D3 structures include non-penetrative faults, veins, and extension fractures. Data from Shaw island were contributed by Kenneth Frank (2015, written communication).

Primary and D1 Structures

A widespread S1 foliation exists within all terranes and dips gently to steeply NE to SW, averaging gently SE (Fig. 2). The S1 slaty-to-phyllitic foliation varies from well-developed to weak and is most pronounced in fine-grained sedimentary rocks (Figs. 3A, 3B). Flattening along S1 is evident by truncated grain boundaries and isoclinal folds of bedding with limbs parallel to the S1 fabric (Fig. 3C). Lineations along S1 foliation planes were not

observed. Bedding and primary structures (S0) exist in most sedimentary units and include graded bedding in sandstones and alternating layers of chert and argillite in ribbon chert units. Bedding is typically parallel to the S1 foliation or is chaotically folded with no surrounding fabric (Figs. 3C, 3D).

Due to a lack of crosscutting constraints, all folds outside of D2 shear zones and not related to D3 faulting are defined here as F1 folds. F1 folds are characterized as either 1) folds of bedding with axial planes parallel or subparallel to S1 foliation, or 2) folds with axial planes not parallel to S1, and lacking axial planar cleavage. Fold axes of folds with S1 axial planar cleavage plunge gently to moderately in most directions (Fig. 4A), are cm- to m-scale, tight to isoclinal, harmonic and disharmonic, and both symmetric and asymmetric. Hingelines of asymmetric F1 folds with S1 axial planar cleavage broadly define a girdle dipping 45˚ SSE and indicate a scattered relationship between clockwise and counterclockwise folds (Fig. 4B). F1 folds lacking axial planar cleavage vary widely in style and orientation (Figs. 3D, 4C).

D1 veins are rare and include extension veins that are cut by and shortened perpendicular to S1. Veins consist of predominantly quartz, calcite, and aragonite with minor lawsonite (Table A1). Two of the four veins sampled contain aragonite (Fig. 5).

D2 Shear Zone Fabrics and Folds

The second deformation event (D2) is defined by brittle-ductile shear zones found both along and near terrane boundaries (Figs. 2, 6, 7, 8, 9). The D2 shear zones studied here were previously mapped by Vance (1975) as the Rosario thrust (Figs. 1B, 2, 9) and a complex “tectonic zone” (Figs. 1B, 2, 7) that lies structurally below the Orcas thrust within

the Turtleback terrane. D2 fabrics dip moderately SE with moderately SE-plunging lineations (Figs. 2, 4D). No shear zones are exposed where the Orcas thrust was mapped by Vance (1975) and are interpreted to be faulted out of view by D3 faults as these locations lack D2 shear zone terrane contacts. Three locations with excellent coastal exposures of structures representative of D2 shear zones on Orcas Island (Figs. 7, 8, 9) were studied in detail.

The tectonic zone near the Indralaya location (Fig. 7) is an imbricate shear zone juxtaposing the older Turtleback Complex above the younger East Sound Group. The D2 shear zones and fabrics steepen progressively from moderately SE-dipping in the south to steeply SE-dipping in the north with consistent down-dip L2 lineations (Fig. 7C). Rigid blocks of Turtleback Complex diorite are separated by ~2 meter-thick serpentine-rich shear zones, whereas deformation in East Sound Group is distributed along numerous basalt-rich cataclastic zones that contain tectonic blocks of limestone, pillow basalt, and volcaniclastic rock (Fig. 7B). Shear sense is dominantly top-to-the-NW thrusting (Fig. 7C).

A zone of imbricate faults at the Otter Bay locality (Fig. 8) is considered here to be part of the Orcas thrust zone as the younger Deadman Bay terrane ribbon chert is faulted above the older Turtleback terrane diorite within the footwall of one strand of the Rosario Thrust. A block of East Sound limestone is faulted into view along an older-on-younger thrust of unknown relative timing to the other thrust. The D2 shear zones and S2 fabrics dip gently east with L2 lineations plunging gently SE (Fig. 8C). Shear sense is dominantly top-to-the-NW sinistral motion along the 1-2 meter thick shear zones located within and between the terranes (Figs. 8B, 8C).

The Rosario thrust at the Ferry location (Fig. 9) imbricates the younger Constitution terrane sandstone above the older footwall Deadman Bay terrane ribbon chert. D3 normal

faults offset the fault contact, but there is evidence for at least two imbricate thrusts (Fig. 9). Strain is focused mostly within the argillite-rich units of the Deadman Bay terrane, with variable amounts of strain within the ribbon chert. S2 fabric orientations dip moderately NE and average L2 lineations plunge moderately SE (Fig. 9C). Kinematic indicators show predominantly top-to-the-NNW, thrust-sense shear (Fig 9C). Slices of the Garrison schist were found faulted into the Rosario thrust zone at a location north of Rosario Resort in East Sound (Fig. 2) but are not present at the Ferry location.

D2 fault zone characteristics provide evidence of brittle-ductile deformation. The shear zones contain argillite- or basalt-rich cataclasite with broken and rotated wall rock fragments (Figs. 6A, 6D). Shear zones contain cm- to m-scale elongate porphyroclasts and blocks that are aligned parallel with fault zone boundaries (Figs. 6A, 6D). A scaly S2 fabric consists of small-scale shear bands spaced mm to cm apart, and is defined by newly grown chlorite and flattened rock and mineral fragments (Figs. 6C, 6D, 10). A widely-spaced cleavage (~10 cm) occurs locally in argillite-rich ribbon chert (Fig 6C). Typically, the S2 fabric contains S and C planes similar to ductile shear zone fabrics, with C-planes defining the overall orientation of the shear zone (Fig. 6C).

F2 folds exist within D2 shear zones and bend S1 into S2 along shear zone boundaries and along the edges of blocks within shear zones (Figs. 6C, 6E). F2 fold axes plunge gently to moderately and broadly define a girdle dipping 38˚ to the SE (Fig. 4E). F2 folds are dm- to cm-scale, tight to isoclinal, harmonic and disharmonic, and parallel and similar.

Outcrop- and microscopic-scale shear sense indicators show the sense of slip along D2 shear zones. L2 lineations are defined by slickenlines and elongated porphyroclasts, and agree with the slip directions calculated from brittle-ductile S/C fabrics and Riedel shears (Figs. 6D, 6F). Asymmetric porphyroclasts of basalt and sandstone are common in cataclastic-rich sections of D2 shear zones (Figs. 6A, 6D). F2 folds verge NW-NE (Fig. 4E). A predominant top-to-the-NW shear sense is evident within each D2 shear zone and collectively (Figs. 4D, 4E, 7C, 8C, 9C). Opposing thrust and normal shear sense along SE-dipping shears is common. Additionally, NW-dipping normal-sense shears are found within zones dominated by SE-dipping thrust-sense shears. Microstructures indicate similar relationships (Fig. 10).

D2 veins are rare on Orcas Island and include mm- to cm- thick shear veins parallel to the S2 fabric. The two veins sampled contain both aragonite and quartz (Fig. 5), with one sample also containing calcite.

Post-cleavage Brittle Deformation

Post-cleavage brittle faults (D3) cut D1 and D2 structures everywhere and have meter-scale offsets and centimeter- to meter- spacing (Figs. 7B, 8B, 9B, 11). D3 fault types are grouped using crosscutting relationships, fault orientation, lineation rake, and sense of shear. For simplicity, D3 faults are classified into dip-slip and strike-slip; faults with lineations raking $\leq 45^{o}$ are considered strike-slip, and those $>45^{o}$ are considered dip-slip. Mutual crosscutting relationships between normal, reverse, and strike-slip faults were observed in outcrop (Fig. 12).

D3 faults have consistent fault rock characteristics but vary in sense of slip and orientation. D3 fault zones range up to 20 cm thick but are more typically discrete slip planes (Figs. 11A, 11D). Normal faults are the most common D3 structure (67% of faults) and dip in all directions, with two modes dipping moderately SE and gently to moderately NW (Figs. 12A, 12B). Strike-slip faults (23%) dip moderately to steeply in all directions (Fig. 12D). Thrust faults are the least common D3 structure (10%) and dip either gently to steeply NNE and SSW or moderately to steeply E and W (Fig. 12G).

Shear veins are commonly associated with D3 faults. Veins accompany ~50% of normal faults, ~65% of strike-slip faults, and ~80% of thrust faults. Veins contain quartz, calcite, and aragonite, are up to 5 cm thick, and lie along the fault planes (Fig. 11C). Eight of the 17 veins sampled contain aragonite (Fig. 10). Roughly half of the D3 normal and strike-slip related veins contain aragonite, while D3 thrust faults contain only calcite (Fig. 10). The overall vein mineralogy varies locally with the surrounding rock type; veins are typically quartz-rich when cutting chert, argillite, or sandstone units and carbonate-rich when cutting basalt or limestone units.

INTERPRETATION OF STRUCTURES

Original Orientation of Structures

The following discussion assumes that the D1-D3 structures have not been considerably reoriented since formation. The large-scale geometry of the Orcas and Rosario thrusts (Fig. 1B) suggests the presence of gentle, km-scale SE-plunging folds in the SJTS, which implies folding after D2. However, the relative age of the km-scale folding and D3 structures is indistinguishable both in the field and by structural analysis. Systematic folding of D3 fault kinematics could not be assessed because structures were measured mainly in the

hinge of the large SE-plunging synform, rather than in fold limbs (Figs. 1, 2). Unfolding of S1 and S2 is impossible without constraints on their original orientations, as the fabrics were likely not horizontal during any initial deformation. However, the effects of folding on the interpreted shear sense for D2 of this study are considered minimal in the immediate study area because data were gathered near the hinge of the km-scale fold, and the SE-plunging fold axes of the km-scale folds are parallel with the majority of L2 lineations. This geometry would result in little rotation of L2 (Fig. 4D). Folding is therefore tentatively considered D4 rather than D3.

Paleomagnetic studies suggest clockwise rotations of crustal blocks along the western edge of the North American Cordillera (Beck et al. 1981; Irving, 1985; Cowan et al., 1997; Housen et al., 2003). Magnetic resetting is thought to have been widespread in rocks of the SJTS during the Cretaceous normal Superchron (118-83 Ma), and magnetic declinations now show significant deviations from the “expected” Cretaceous orientations. Work by Burmester et al. (2000) and Schermer et al. (2007) highlights the issues involved with producing accurate paleomagnetic reconstructions of the SJTS. Without constraints on the folding of S1 and S2, it is impossible to determine the amount of scatter caused by the folding event(s) (Burmester et al., 2000). Additionally, Schermer et al. (2007) explain that between some outcrops, paleomagnetic orientations are similar while late brittle structures are scattered, whereas at other locations, the opposite is true. Therefore, the relative age of the paleomagnetic signature is not well constrained, making paleomagnetic reconstructions uncertain. Thus, D1-D3 structures presented here are considered to be in their original orientations.

D1 Flattening Fabric

The S1 foliation is interpreted as a flattening fabric with a Z-axis plunging moderately to the NW. Shortening perpendicular to the S1 foliation is interpreted to result from solution mass transfer (SMT), as evident by truncated grains and aligned micas along S1. The lack of S1 foliation in massive sandstones indicates a varying degree of fabric development during S1 formation. Shearing during the D1 event is considered unlikely given the absence of lineations or other kinematic indicators along the S1 fabric.

Folds of bedding are interpreted to result from D1 flattening (F1) and pre-S1 deformation of uncertain significance. One interpretation of the chaotic folding of ribbon chert bedding is soft sediment slumping prior to S1 fabric formation. Asymmetric F1 folds with S1 axial planar cleavage do not define an axis of symmetry along a girdle representative of a shear zone, again suggesting flattening rather than shear (Fig. 4B).

Assembly along Imbricate D2 Shear Zones

Imbricate D2 shear zones are interpreted to be the faults responsible for the assembly of terranes on top of one another into their current nappe stack. D2 fabrics are concentrated along terrane boundaries, suggesting that D2 was responsible for terrane assembly. The abundant lineations, asymmetric fabrics, and fault-propagation folds associated with D2 shear zones represent non-coaxial strain (Fig. 6). The severely fragmented fault rock, overall thickness of the shear zones, and presence of exotic fault slices (e.g. Garrison Schist) indicate that significant offset was accommodated along these structures. However, slip along individual shear zones is likely considerably less due to the number of shears. Evidence of the Orcas thrust within the imbricated section of the Rosario thrust at Otter Bay (Figs. 2, 8A,

8B) suggest that the Rosario thrust cuts the Orcas thrust and either roots into the Turtleback terrane, or reactivates an older on younger thrust.

Shear sense is interpreted to be dominantly N- to NW-directed during terrane assembly. Sixty-six shear sense features indicate top-to-the-N or NW motion, and eight indicate top to SE (Figs. 4D, 4E). I suggest these opposing shear sense indicators are due to a flattening component together with non-coaxial shear. In this interpretation, SJTS terranes must have been located separately somewhere south along the continental margin prior to the D2 thrusting event.

Kinematics of Post-Cleavage Faulting

Post-cleavage faults with slip sense data were analyzed using FaultKinWin (Allmendinger, 2016) to determine the principal strain axes for each D3 fault set. FaultKinWin estimates the compression and tension axes (equivalent to compression and tension axes for earthquakes) for each fault using fault orientation, lineation orientation, and slip sense (Marrett and Allmendinger, 1990). Fault trace lengths and displacements are generally not observable on Orcas and Shaw Islands, therefore D3 structures were weighted evenly and kinematic axes were calculated using the linked Bingham analysis (Allmendinger, 2016).

Kinematics of D3 structures are variable, but are dominated by NW-SE extension. Analysis of D3 normal faults indicates overall NW-SE subhorizontal extension (Fig. 12C). The predominance of SE-dipping normal faults suggests preferential faulting down to the SE. Analysis of D3 strike-slip faults shows mixed subhorizontal extension and shortening in all directions (Fig. 12E). No significant crosscutting or conjugate fault relationships are

distinguishable (Fig. 12F). Analysis of D3 thrust faults shows a weak cluster of gently S-plunging compression axes, suggesting N-S shortening during faulting (Fig. 12H). However, the small sample size of D3 thrust faults makes the significance of this fault set uncertain. Given the uncertainty in D3 thrusts, the lack of well-defined strain axes for D3 strike-slip faults, and the predominance of normal faulting during the D3 event, the stress field is interpreted as dominantly NW-SE extension with subvertical shortening during D3. The mutual crosscutting relationships between D3 normal, strike-slip, and thrust faults are interpreted to result from spatial and temporal overlap of small-scale structures formed in a locally heterogeneous stress field (e.g., Sassi and Faure, 1997; Maerten et al., 2002).

INTERPRETATION OF PRESSURE AND TEMPERATURE CONDITIONS

Pressure and temperature conditions for Orcas and Rosario thrusts are broadly constrained by vein mineralogy and D2 fault rock microstructures. Aragonite was found in structures of all ages in this study (Fig. 10). Lawsonite was only found in one D1 vein sample in this study, but has been reported along with aragonite in deformed veins overprinted by foliation and in veins that crosscut foliation and brittle-ductile shear zones (D2 of this study) (Brandon et al., 1988; Maekawa and Brown, 1991; Cowan and Brandon, 1994; Bergh, 2002). The cross-cutting veins are likely related to the prominent NE-SW striking D3 normal faults reported here, as Maekawa and Brown (1991) describe them as being perpendicular to a NW-SE stretching lineation. Therefore, the peak metamorphic assemblage of aragonite + lawsonite is interpreted to be relatively stable from D1 through at least part of the D3 deformation, and roughly constrains temperatures from 125 - 300˚C (Boettcher and Wyllie, 1968; Crawford and Hoersch, 1972; Frey et al., 1991). The evidence of intergranular slip and lack of

recrystallization of quartz in D2 shear zones limit maximum temperatures to <250˚C (Simpson and De Paor, 1993; Stipp et at., 2002). Furthermore, Carlson and Rosenfeld (1981) suggest that the preservation of aragonite is very unlikely when exhumed from temperatures higher than 200˚C. Pressure stability of aragonite at temperatures of 200 - 250˚C requires minimum pressures of 5.5 - 6.6 kbar (Boettcher and Wyllie, 1968; Crawford and Hoersch, 1972). Consequently, P-T conditions are interpreted here to be relatively stable from D1 to D3 deformation at ~200˚C and ≥5.5 kbar.

DISCUSSION

The structural and metamorphic history interpreted above suggest that rocks on Orcas and Shaw Islands were affected by several stages of deformation, and has implications for models proposed by previous workers in the SJTS. First, discrepancies between the number and timing of fabrics proposed here and by previous workers are addressed (Table 1) (Brandon et al., 1988; Maekawa and Brown, 1991, 1993; Bergh, 2002). The kinematics of D2 shear zones are then compared and contrasted to those used to produce previous models of mid-Cretaceous thrusting in the SJTS (Brandon et al., 1988; Maekawa and Brown, 1991, 1993; Cowan and Brandon, 1994; Bergh, 2002). Previous accounts of HP-LT mineralogy and the interpreted significance for models of the SJTS (e.g., Glassely et al., 1976; Brandon et al., 1988; Feehan and Brandon, 1999) are considered in light of the new evidence for aragonite in late (D3) brittle structures. Lastly, the significance of margin-parallel extension and the scatter of kinematics during D3 are discussed.

Implications for Cretaceous Models of the SJTS

Fabric Development and Associated Kinematics

Previous work in the SJTS resulted in three hypotheses regarding the timing and number of fabrics (Table 1). Brandon et al. (1988), Cowan and Brandon (1994), and Feehan and Brandon (1999) argued for two fabrics; a cataclastic fabric located within terrane assembly fault zones (the first event of their study, but D2 of this study), and a later SMT fabric that overprints the cataclastic fabric and surrounding terranes during exhumation of the SJTS (Brandon et at., 1994). Maekawa and Brown (1991) cite the near-parallel relationship and similar metamorphic signature of these two fabrics as evidence for only one fabric-forming event. Lastly, Bergh (2002) suggested that an early fabric (S1) is equivalent to both the cataclastic and SMT fabrics discussed by Brandon et al. (1988), and is followed by a second, roughly parallel shear fabric (S2) found within terrane-bounding shear zones (e.g., Rosario thrust and LSC).

Several kinematic models have been proposed for the SJTS using the interpretation of structures similar to D2 of this study. Expanding on the fold analysis of Hansen (1971), Cowan and Brandon (1994) assumed that all folds and cataclastic shear zones were synchronous and that a systematic relationship exists among folds and shear zones that warrants the interpretation of overall SW-directed shearing and subvertical flattening during terrane assembly related to collision of Wrangellia with North America. Conversely, Maekawa and Brown (1991) interpreted these folds, along with abundant SE- and NW-plunging lineations and shear fabrics, as the result of dominantly NW-directed subsimple shear during translation of terranes and emplacement over Wrangellia. The kinematic model of Bergh (2002) combined the NW- and SW-directed interpretations. Bergh (2002) suggested

that SW-directed thrusting was accommodated within the Rosario fault zone during D1, citing consistent asymmetric folds with an axial planar cleavage and lineations of stretched chert lenses, sandstone lenses, and quartz ribbons. Bergh (2002) further proposed that during D2, oblique subduction of the Farallon Plate produced NW-directed structures similar to the shear fabrics described by Maekawa and Brown (1991).

The D1 and D2 structures interpreted in this study are inconsistent with some of the previous interpretations of the fabrics and kinematics in the SJTS. Brittle-ductile shear zones cut and drag foliation from the surrounding wall rock and along blocks within the D2 shear zones, and require two temporally distinct fabrics despite their regionally subparallel orientation (Figs. 6A, 7B, 8B, 9B). The lack of shear indicators along S1 fabrics within brittle-ductile shear zones that separate terranes indicate that D1 cannot be responsible for terrane assembly. Evidence of SW-directed thrusting (Brandon et al., 1988; and Cowan and Brandon, 1994; Bergh, 2002,) was not found on Orcas and Shaw Islands. Folds within and adjacent to D2 shear zones are not SW-vergent, nor are they systematically oriented to have been formed by SW-directed shearing (Figs. 10A-C). If SW-directed motion was accommodated along the brittle-ductile shear zones prior to D2 (as in Bergh, 2002), then evidence along the Rosario thrust on Orcas and Shaw Islands may have been completely erased during NW-directed thrusting. Therefore, kinematics during the D1 of Bergh (2002) cannot be assessed. My interpretation of NW-directed shear along the imbricated D2 shear zones is consistent with the model of margin-parallel translation during oblique subduction as proposed by Maekawa and Brown (1991) (Fig. 13). The oblique component of traction on the base of the forearc by the subducting plate may have led to the translation of nappes as

forearc slivers into a reentrant formed by the protruding Coast Plutonic Complex and already accreted Wrangellia, as proposed by Brown (2012) (Fig. 13).

Relative Timing of HP-LT Metamorphism

The timing of peak metamorphism relative to deformation has been interpreted differently by previous workers, leading to disagreement over which structures record deformation within the accretionary wedge setting. Orogen-normal contractional models (Brandon et al., 1988, 1993, 1994; McGroder, 1991; Cowan and Brandon, 1994; Feehan and Brandon, 1999) cite static veins of aragonite, lawsonite, and prehnite and deformed veins of lawsonite as evidence that HP-LT metamorphism postdates major slip along cataclastic shear zones (D2 of this study), and largely predates SMT cleavage formation (S1 of this study). Maekawa and Brown (1991, 1993) interpreted similar evidence to show that HP-LT conditions are coeval with faulting and fabric formation (D1 and D2 of this study), suggesting that terranes were assembled and thrust over Wrangellia during HP-LT conditions. The obduction model of Brown (2012) revised the interpretation of syn-thrusting HP-LT metamorphism and states that metamorphism ended prior to assembly. Brown (2012) proposed that assembly related shear zones are non-metamorphic, young upward, and separate terranes that have different metamorphic histories acquired independently before their assembly during thrusting over Wrangellia.

The vein mineralogy of D3 structures requires a reassessment of models that argue for assembly faults post-dating metamorphism. Aragonite in D3 structures (and equivalent structures of Schermer et al., 2007) shows that HP-LT conditions likely continued after terrane assembly. HP-LT metamorphism is not reported for rocks of Wrangellia (e.g.,

Surdam, 1973), making it unlikely that the HP-LT faults of the SJTS formed above the southern edge of Wrangellia. The post-cleavage aragonite also invalidates the interpretation that the SMT fabric formed after HP-LT metamorphism, during exhumation (Feehan and Brandon, 1999). Structures related to exhumation must be either late D3 faults lacking a HP-LT signature (Fig. 5), or structures preserved elsewhere. These findings also suggest that the faults related to emplacement of HP-LT terranes as hanging wall to Wrangellia are yet to be discovered (Fig. 13). Perhaps the many waterways, Eocene sedimentary rocks, or Quaternary cover proximal to the San Juan Islands conceal the final emplacement structures (Fig. 1).

Evidence of pre-assembly thrusting?

The fault contact between the Turtleback Complex and East Sound Group on Orcas Island represents one of the few old-on-young thrust contacts in the SJTS. Brandon et al. (1988) and Brown and Gehrels (2007) interpreted these two units as the same terrane, and suggested that the East Sound volcanics were deposited over the Turtleback plutonic rocks in an arc-volcanic setting. Map evidence (Figs. 1, 2) suggests a major thrust contact, as the Turtleback Complex now lies structurally above the East Sound Group. This thrust, in addition to the Orcas thrust, is cut by the Rosario thrusts (Fig. 2). Brown (2012) interpreted the SJTS nappes as forearc slivers originating somewhere south along the Cordilleran margin, and other workers have noted correlations between rock units in the SJTS with terranes in the Klamath Mountains (Cowan, 1980; Brown, 1987; Brandon et al., 1988). These hypotheses suggest that this old-on-young fault may represent a pre-assembly thrust. However, the NW-SE oriented lineations, top-to-the-NW shear indicators, and the SE-dipping imbricate nature of brittle-ductile shear zones separating the two terranes at Indralaya

(Figs. 2, 7) are similar to D2 deformation discussed above. Without age constraints for this fault, I interpret juxtaposition of the East Sound Group and Turtleback Complex to have occurred during the D2 assembly, but prior to emplacement of Constitution terrane along Rosario thrust.

Origin of D3 Structures

Late brittle structures presented here signify the beginning of vertical shortening and horizontal extension. A predominance of margin-parallel extension similar to D3 structures described here and in Schermer et al. (2007) has been observed at locations with oblique convergence (e.g., Aleutians and Sumatra (McCaffrey, 1992 and 1996; Avé Lallemant and Oldow, 2000); the High Himalayas (Styron et al., 2011), Ryukyu arc (Kuramoto and Konishi, 1989); and the Cretaceous plate margin of Venezuela (Avé Lallemant and Guth, 1990)). Avé Lallemant and Guth (1990) showed that margin-parallel extension may result from an increased margin-parallel component of slip along the length of a curved margin. However, the component of extension not parallel to the margin may instead signify internal adjustment of the wedge in response to overthickening during previous thrusting, additional underplating, or a combination of both (e.g., Platt, 1986; Carmignani and Kligfield, 1990; Wallace et al., 1993). Late brittle structures in the LSC reported by Gillaspy (2004) indicate orogen-normal thrusting prior to normal faulting in the SJTS. The predominance of orogen-parallel extension may then represent the presence of a weak or nonexistent lateral buttress to an overthickened wedge. The evidence presented in this study can not distinguish the primary cause of D3 deformation.

The scatter of D3 kinematics may be the result of spatial and temporal variation in the regional and local stress tensors, mechanical interaction of closely spaced faults, and/or the inability to recognize separate post-cleavage events. Scatter of kinematics for each D3 structure type could be related to the assumptions inherent to calculations of stress and strain directions. These assumptions typically include; 1) that there is homogeneous stress field where a group of faults are responding to a single stress orientation, and 2) that there is independent slip in which separate faults are not mechanically interacting (Wallace, 1951; Bott, 1959). Competency contrasts between different lithologies, preexisting layering within variably oriented rocks, and the close spacing of D3 faults on Orcas and Shaw Islands challenge these assumptions (Belanger, 2008). Additionally, it is possible that a homogeneous stress field during a single deformation event produced more than one structure type (e.g., normal and strike-slip). Earthquake focal mechanisms from historic seismic data and structural data gathered from recent coring investigations show that active faults in modern accretionary wedges can have mixed kinematics (e.g. Hayman et al., 2012). This scatter could make the identification of separate events with similar deformation styles difficult using crosscutting relationships alone. If the kinematics related to each event were variable, it would be difficult to distinguish events using structural analysis.

The transition from brittle-ductile (D2) to brittle (D3) structures reflects a change in rheology and fault-fluid relationships in an evolving accretionary wedge. Temperature changes are often associated with varying deformation styles, although the interpretation of relatively constant temperatures (~200˚C) from D1-D3 indicate other controls on rheology. The shift from NW-directed thrusting during D2 to vertical thinning and horizontal extension

during D3 certainly reflect changing boundary conditions and/or plate interactions. Higher strain rates may have been associated with the onset the new D3 stress field. Additionally, strain hardening due to the loss of porosity during previous SMT may have caused the shift to brittle fault behavior (e.g., Moore and Byrne, 1987).

SUMMARY AND CONCLUSIONS

Structures on Orcas and Shaw Islands reveal a sequence of three main deformation events during the mid-Cretaceous orogeny in the Pacific Northwest. The widespread fabric found within terranes lacks evidence of non-coaxial strain and is interpreted as an SMT flattening fabric imprinted during initial accretion of the terranes to the continental margin. Brittle-ductile D2 shear zones several meters thick cut the flattening fabric and imbricate rocks both along terrane contacts and within the terranes themselves. The D2 shear zones are the main structures of the SE-dipping San Juan thrust system and are interpreted to accommodate slip during assembly of the SJTS nappe stack. Thrusting is dominantly top-to-the NW and is interpreted to result from the translation of terranes northward along the continental margin into a transpressive stepover zone during oblique subduction as argued by previous workers (Brown, 1987; Maekawa and Brown, 1991; Brown, 2012). Post-cleavage brittle D3 deformation includes normal, strike-slip, and reverse faults and related veins. Kinematics are mixed for strike-slip and reverse faults, but the predominance of normal faults and their relatively consistent NW-SE oriented tension axes is interpreted to show overall margin-parallel extension and subvertical thinning during D3. The scatter of D3 kinematics may result from spatial and temporal variation in the regional and local stress

field, the mechanical interaction of closely spaced faults, and/or the inability to recognize separate post-cleavage deformation events.

The peak metamorphic assemblage aragonite + lawsonite is preserved in veins related to D1-D3, showing that all deformation discussed above took place within an accretionary wedge setting with relatively stable P-T conditions of ~200˚C and ≥5.5 kbar. The change in deformation styles during stable P-T conditions indicates that there are other controls on rheology during the development of the accretionary wedge such as fluid loss, strain hardening, and/or variable strain rates. Future work should focus on determining what structures accommodated exhumation of the HP-LT SJTS rocks, and determine if those structures are related to the emplacement of the thrust system over the unmetamorphosed Wrangellia terrane.

TABLES

TABLE 1. COMPARISON OF STRUCTURAL STUDIES IN THE SAN JUAN ISLANDS

Study:	Brandon and coworkers. †	Maekawa and Brown (1991, 1993)	Bergh (2002)	Schermer et al. (2007)	This study
Location:	Western San Juan Islands	Western San Juan Islands	Rosario thrust, LSC, western and southern San Juan Islands	LSC and adjacent areas, southern San Juan Islands	Orcas and Shaw Islands, Rosario and Orcas thrusts, Turtleback and Eastsound Terrane contact
Event*					
D1	SW-verging brittle thrusting; Cataclasis, folds, Riedel shears, Later static HP-LT metamorphism.	Not reported.	SW-verging folds with axial plane cleavage (S1), NE-SW stretching lineation (L1), coeval HP-LT metamorphism.	Not studied; "deformed" veins analyzed for aragonite indicate HP-LT metamorphism.	SMT flattening fabric (S1), HP-LT metamorphism.**
D2	SMT cleavage related to uplift, vertical thinning, NW-SE shortening.	NW-verging ductile, brittle-ductile shear zones (S1) with extension and shear lineations (L1), coeval HP-LT metamorphism.	Penetrative left-lateral NW-verging shear zones (S2) subparallel to S1; drag folds. NW-SE stretching and shear lineations (L2), coeval HP-LT metamorphism.	Not studied; "early strike-slip shear" veins analyzed for aragonite indicate HP-LT metamorphism.	NW-verging brittle-ductile shear zones (S2) and shear lineations (L2), HP-LT metamorphism.**
D3	Not reported.	Late brittle structures not analyzed.	Not reported.	NE- and SW-verging thrust cut D1 and D2 fabric. HP-LT metamorphism.	Predominantly NW-SE extension via brittle faults and extension veins, HP-LT metamorphism.**
D4	Minor veining, normal faults, insignificant strain.	Not reported.	Not reported.	NW-SE and NE-SW extension via normal faults and extension veins. HP-LT metamorphism.	Not reported.
D5	Not reported.	Not reported.	Not reported.	Strike-slip faults and brittle-ductile shear zones. Lower pressure than D4.	Not reported.
D6 ?	---- NW-trending folds and dextral strike-slip faults (Eocene?)†† ----				

†Brandon et al. (1988). Brandon et al. (1994), Cowan and Brandon (1994), Feehan and Brandon (1999).

LSC – Lopez Structural Complex; SMT – Solution Mass Transfer; HP-LT (high pressure – low temperature)

*Event numbers do not necessarily correlate with numbers in each reference but are generalized for the entire study area and deformational history.

** Aragonite data are presented in Figure 5.

†† Cowan and Miller (1981); England and Calon (1991); Johnson (1985); Misch (1966); Tabor (1994)

Table modified from Schermer et al., 2007

FIGURES

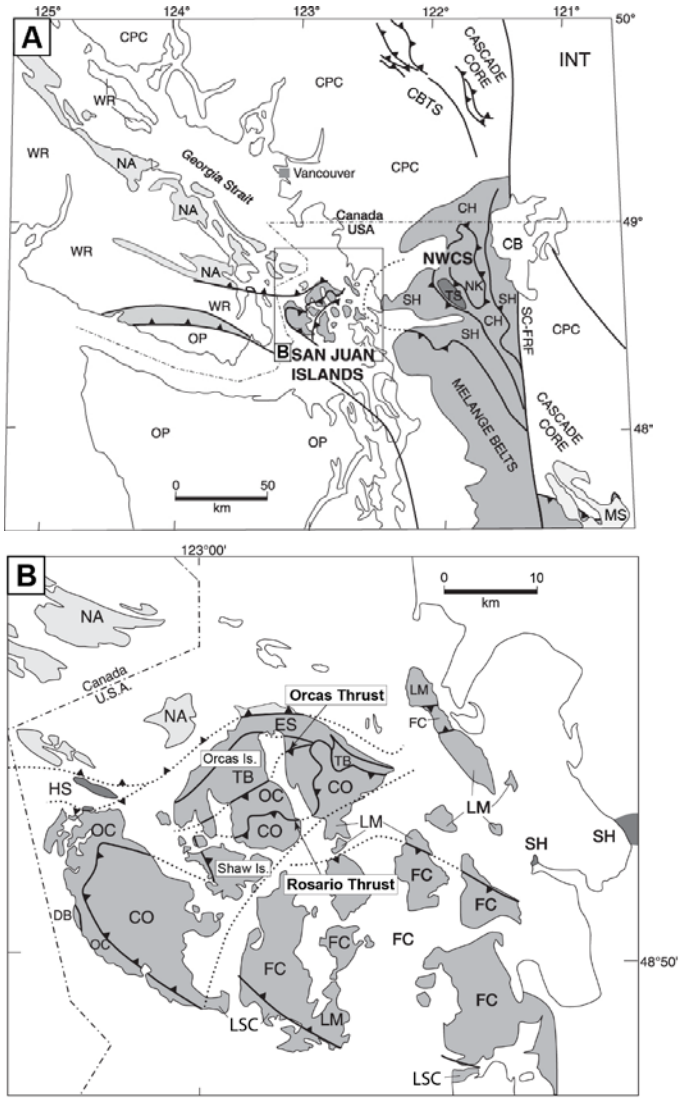

Figure 1. Regional maps showing the geologic setting and rock units of the SJTS. **(A)** Regional map. CB – Chilliwack batholith, CBTS – Coast Belt Thrust System, CH – Chilliwack Group, INT – Intermontane terrane, MS – Mt. Stuart batholith, NA – Nanaimo Group, NK – Nooksack Formation, NWCS – Northwest Cascade system, OP – Olympic Peninsula terranes, SC-FRF – Straight Creek – Fraiser River fault, SH – Shuksan terrane, TS – Twin Sisters Dunite, WR – Wrangellia. **(B)** Rock units and locations of the major terrane bounding thrusts in the San Juan Islands. CO – Constitution Formation, DB – Deadman Bay Volcanics, ES – East Sound Group, FC – Fidalgo Complex, HS – Haro Formation and Speiden Group, LM – Lummi tectonic assemblage, LSC – Lopez Structural Complex, OC – Orcas Chert, TB – Turtleback Complex. White represents Eocene Chuckanut formation or Quaternary cover. Maps are after Brown et al. (2005), and Brown and Dragovich (2003).

Figure 2. Map of terranes and major fault zones on Orcas and Shaw Islands. Equal area stereonet plots show S1 and S2 fabric orientations (black and red lines, respectively) and L2 lineations (red dots) from locations near major fault zones. Plot of poles to all S1 fabrics with 1% area contours is located in the upper left corner. Contour interval is 2%. Locations of vein samples containing aragonite are plotted and colored according to their associated deformation phase. Sample numbers located in table A1. Kenneth Frank (2015, written communication) provided data for Shaw Island. The Tectonic Zone is mapped after Vance (1975).

Caption on previous page.

Figure 3. Photographs of D1 structures. **(A)** Weakly-defined S1 foliation in Constitution terrane sandstone. D3 quartz extension veins cut the S1 fabric at a high angle. Pencil for scale. Site 34. **(B)** Well-defined S1 foliation in ribbon chert from the Deadman Bay terrane. Site 44. **(C)** Chaotic F1 folds in Deadman Bay terrane ribbon chert that lacks axial planar cleavage and show varied fold axes and axial plane orientations. Site 51. **(D)** D2 shear zone separating Turtleback terrane diorite from Deadman Bay terrane ribbon chert. The S1 fabric in the ribbon chert is sub-parallel the D2 shear zone. A carbonate D1 vein is cut by a D2 shear zone. Chisel for scale. Site 55. **(E)** Folded S0 bedding with a well axial planar S1 cleavage in Orcas Chert ribbon chert. Site 33.

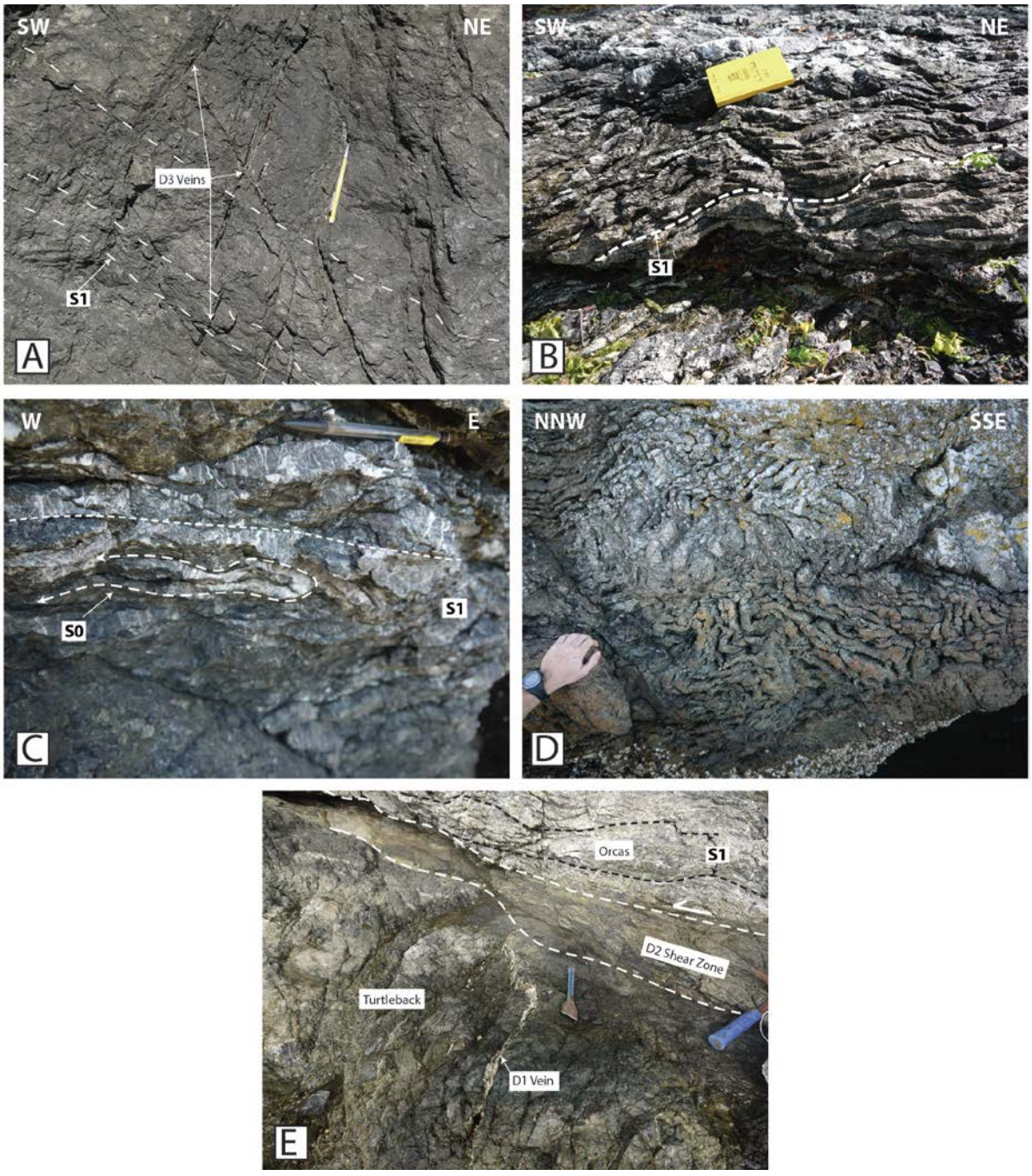

Caption on previous page.

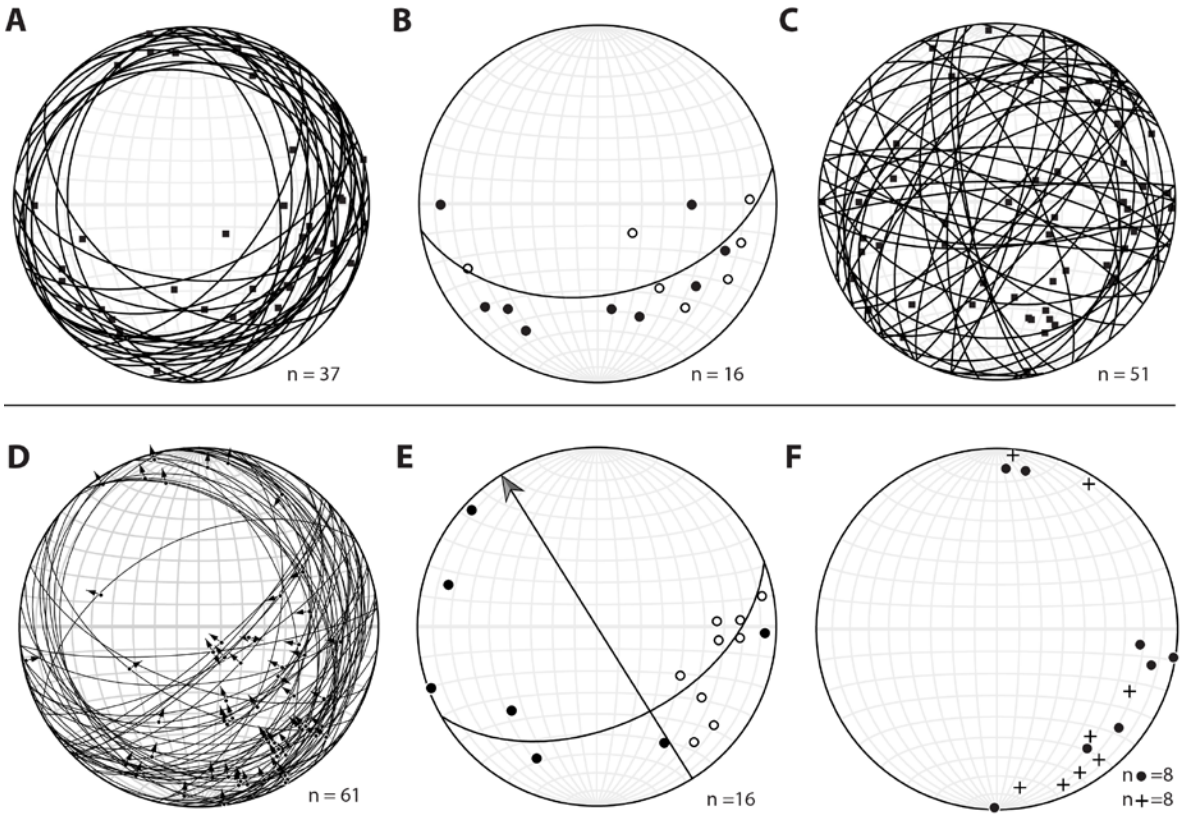

Figure 4. Equal area stereonets of D1 and D2 structures. **(A)** F1 fold axes of folds with axial planes parallel or subparallel to S1. **(B)** Hingelines of asymmetric F1 folds with axial planes parallel or subparallel to S1. Open circles = counterclockwise vergence, solid circles = clockwise vergence. **(C)** F1 fold axes of folds with axial planes not parallel to S1. **(D)** D2 C-plane fabrics and L2 lineations with arrows showing sense of slip. **(E)** F2 fold axes. The great circle represents the best-fit girdle for fold axes, and the arrow points in interpreted direction of shear. Open circles = counterclockwise vergence, solid circles = clockwise vergence. **(F)** Plot comparing lineations calculated from S-C fabric geometries (dots) and lineations measured along S2 C-planes (+). Each line plotted for measured lineations (+) represents the average orientation of lineations at locations in close proximity to where S-C geometries were measured.

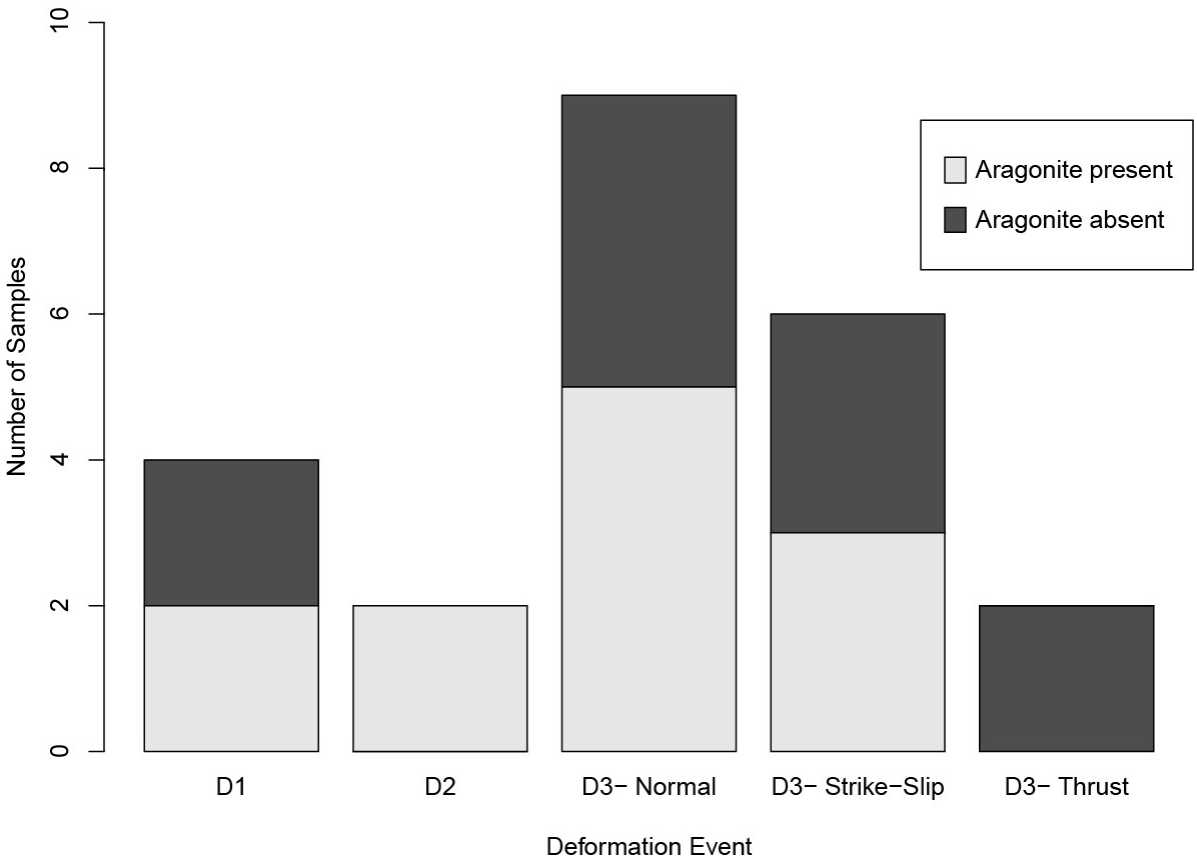

Figure 5. Stacked bar plot representing the number of vein samples interpreted to contain aragonite based on XRD analysis. Results are plotted according to their deformation event. D3 veins are separated into the three main structure types discussed in the text.

Figure 6. Photographs of D2 structures. Site numbers shown on figure A1. **(A)** Lens-shaped block of limestone within the Rosario thrust shear zone on Shaw Island. Many smaller

porphyroclasts of limestone are found throughout the shear zone. Site 55. **(B)** Centimeter-scale D2 shear zone separating ribbon chert from Constitution terrane sandstone. The ribbon chert may either be a slice of the Deadman Bay terrane or the Constitution terrane; this shear is found structurally above the Rosario thrust on Orcas Island. The S1 fabric within the ribbon chert is subparallel to S2. A D3 normal fault offsets the D2 fault contact. Site 24. **(C)** Brittle-ductile fabrics (S, C, and Riedel) typically found within D2 shear zones. The S1 fabric is clearly cut and bent by the D2 shears. Brunton for scale. Site 37. **(D)** D2 shear zone near Indralaya containing porphyroclasts of wall rock fragments from the East Sound Group (basalt, limestone, and volcaniclastic sandstone) within basalt-rich cataclasite. Shear sense is top-to-the NW. Site 39. **(E)** Rosario fault zone (D2) showing the S1 fabric cut and dragged along D2 shears. Folds and asymmetric ribbon chert porphyroclasts show top-to-the NW shear. Site 69.

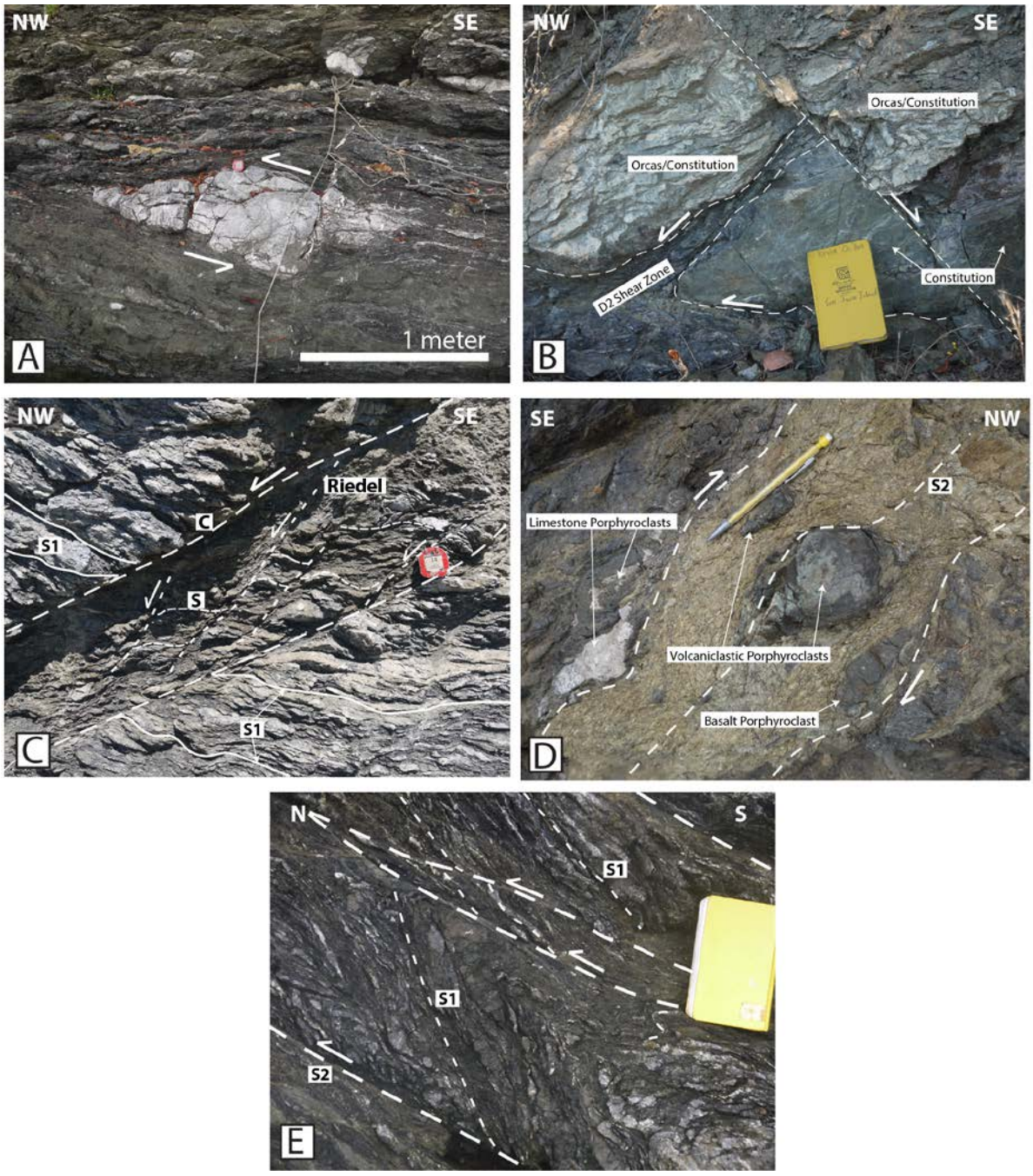

Caption on previous page.

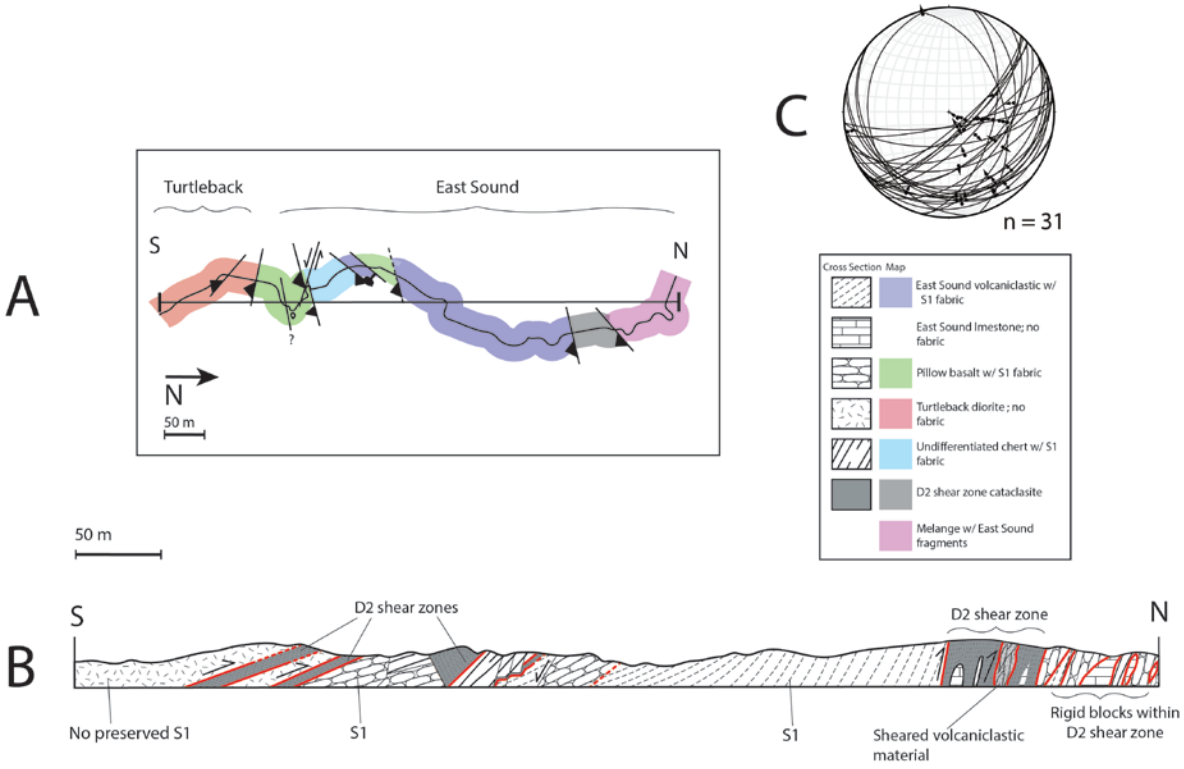

Figure 7. Imbricate faulting between the East Sound Group and the Turtleback Complex near Indralaya (Indralaya; Fig. 2). (A) Geologic map of the coastline. (B) Cross-section; description as in figure 7B. (C) Equal-area stereonet of S2 and L2; description as in figure 7C.

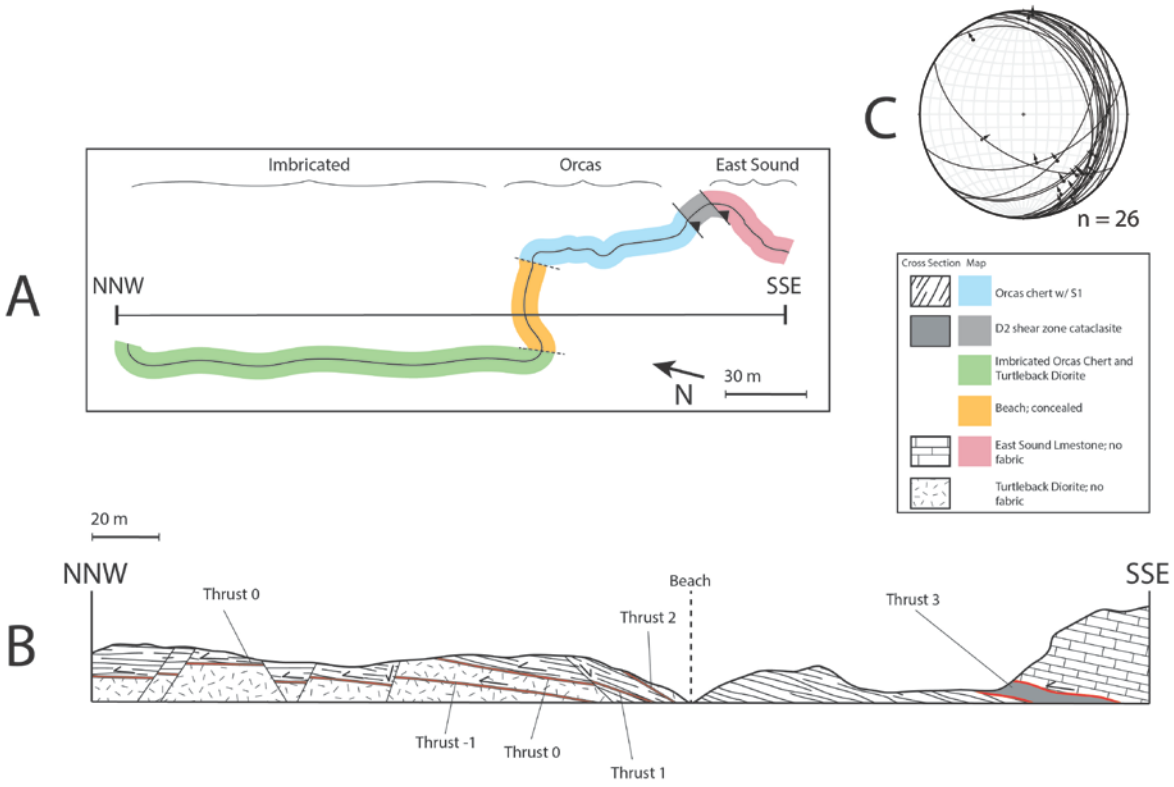

Figure 8. Orcas thrust imbricating the Turtleback and Deadman Bay terranes at Otter Bay (Otter Bay; Fig. 2). (A) Geologic map of the coastline. (B) Cross-section; description as in figure 7B. Faults are numbered in order from structurally lowest to highest, with thrust 0 representing the contact between the two terranes. (C) Equal-area stereonet of S2 and L2; description as in figure 7C.

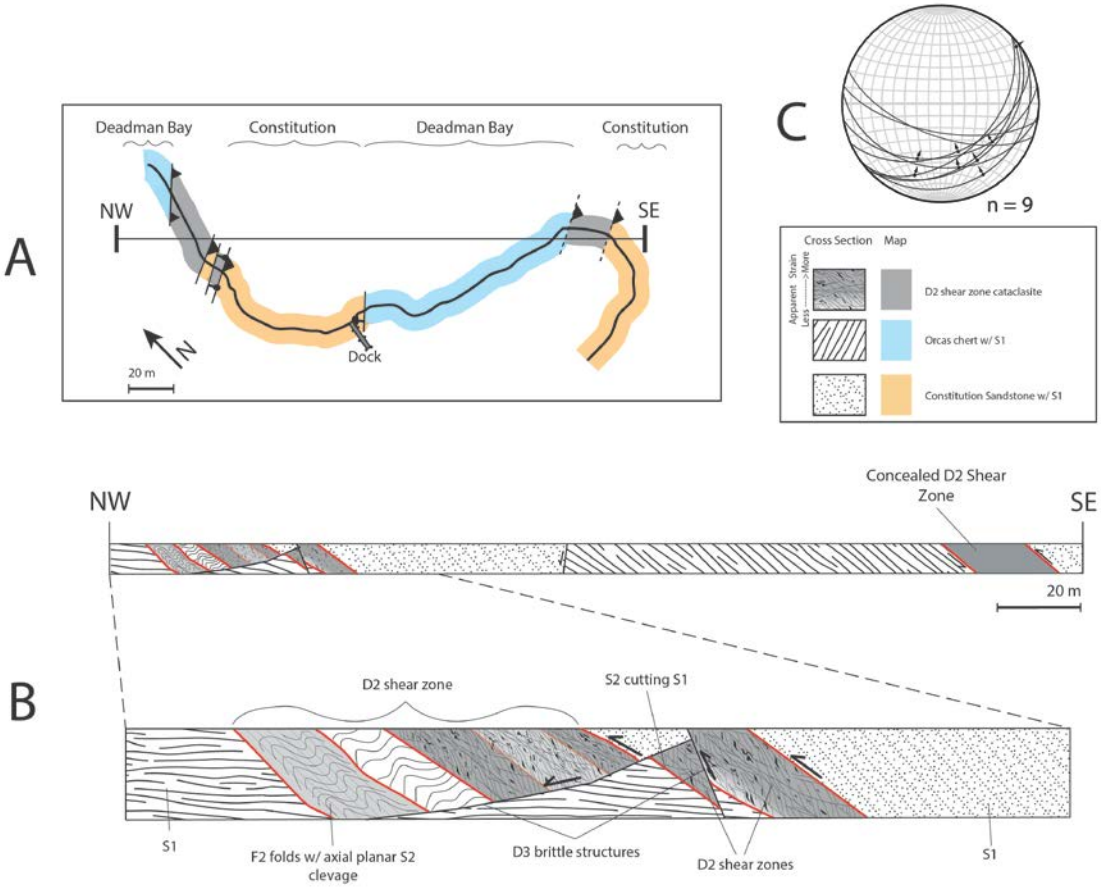

Figure 9. Rosario thrust near the Orcas Island Ferry (Ferry: Fig. 2). (A) Geologic map of the coastline showing the contact of Constitution Formation and Orcas Chert. (B) Cross-section. Cross-sections in figures 7-9 are produced from coastline sketches and measurements of faults and fabrics. Only major D3 faults are shown for each locality. No vertical exaggeration. (C) Equal area stereonets in figures 7-9 show D2 C-plane fabrics and L2 lineations with arrows indicating the sense of slip.

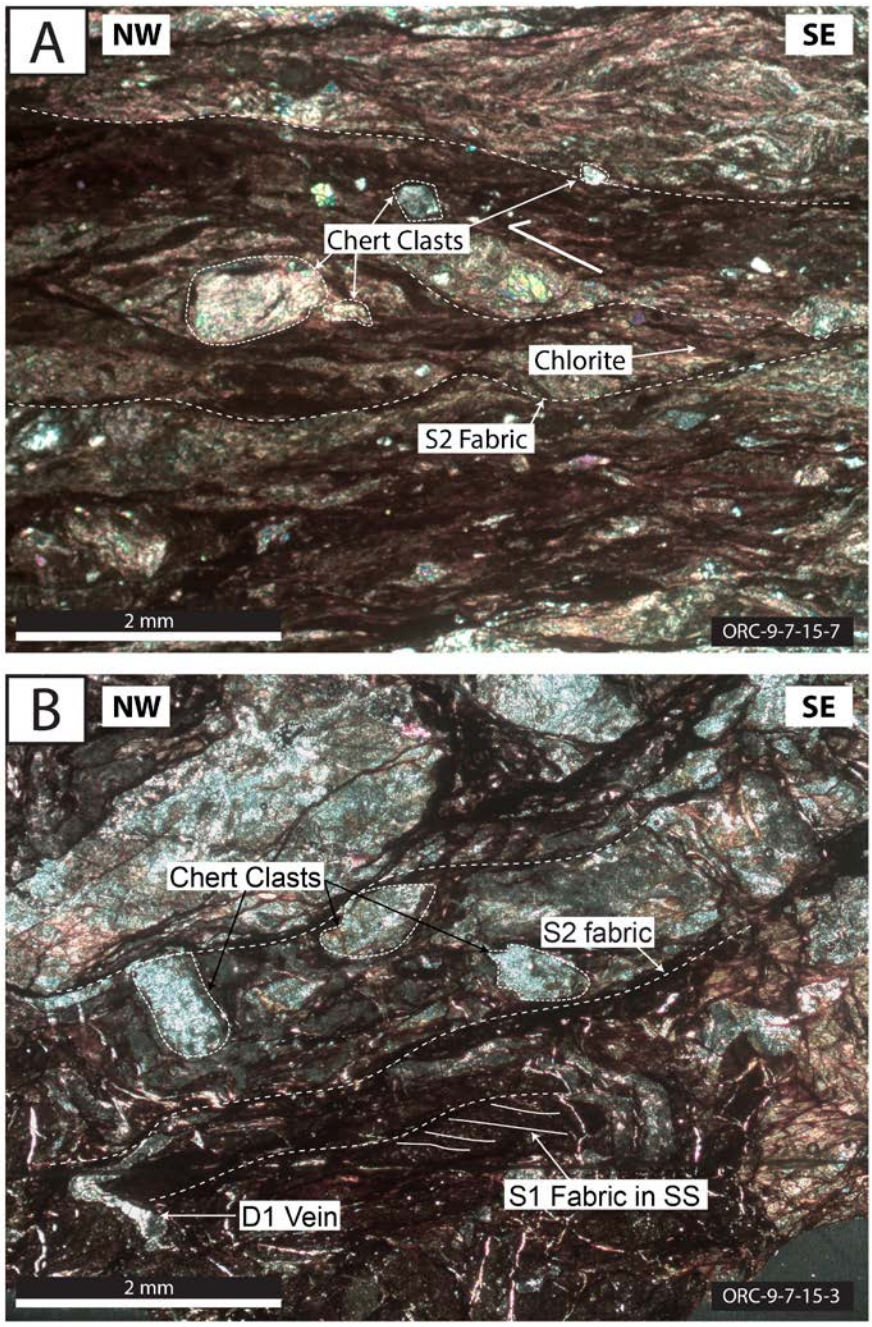

Figure 10. Photomicrographs showing asymmetric fabrics within D2 shear zone rocks. Shear sense is top-to-the northwest in both images. Cross-polarized light. **(A)** Sigmoidal wall rock porphyroclasts, S-C foliations, broken and rounded wall rock fragments of chert, and shear bands. **(B)** Shear bands, broken and rounded wall rock fragments of chert, and a cut and dragged quartz vein that truncates the S1 fabric in sandstone (SS) wall rock fragments.

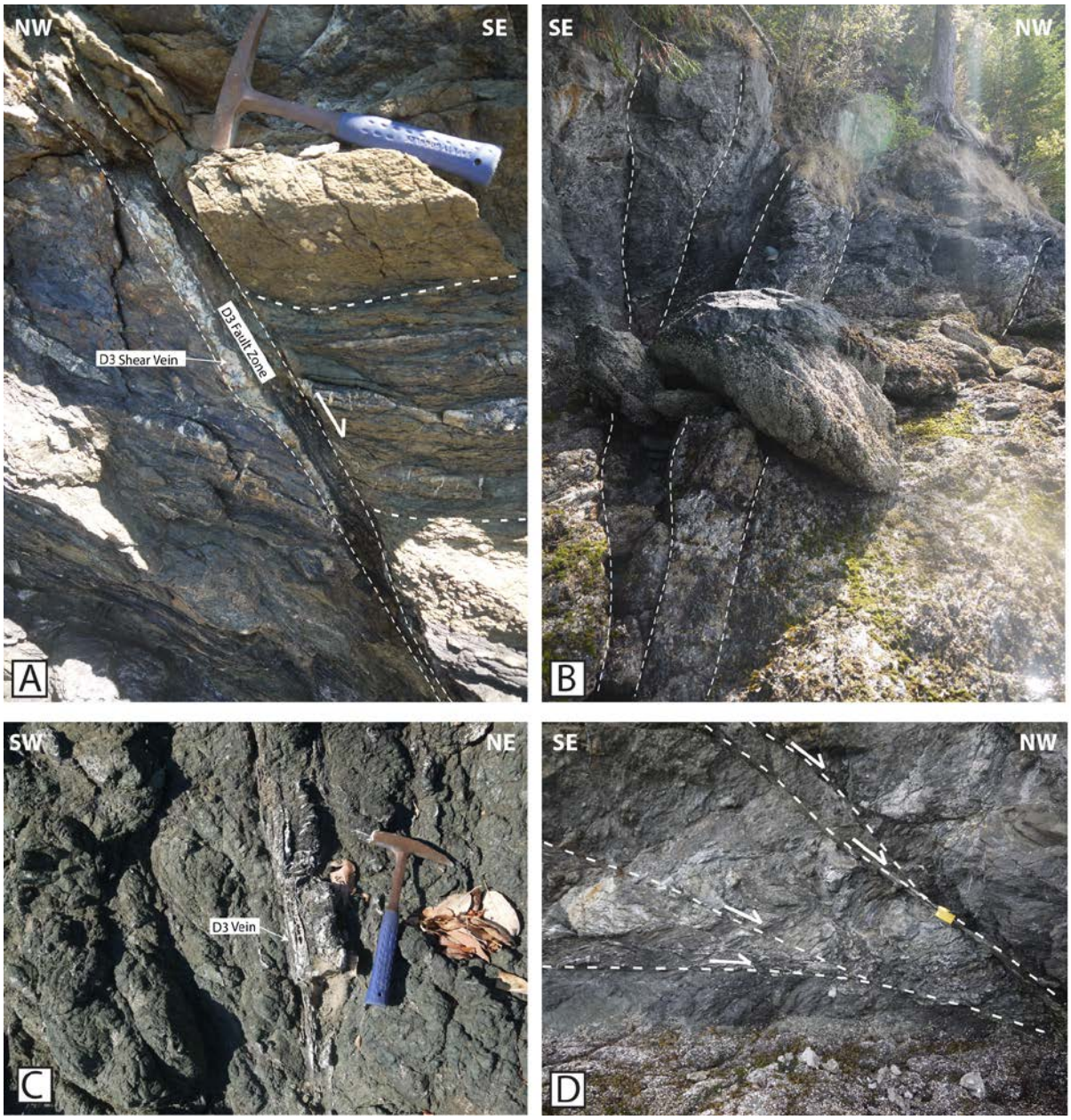

Figure 11. Photographs of D3 structures. Faults are outlined by dashed lines. Site numbers shown on figure A1. **(A)** D3 normal fault cutting a D2 shear zone. D3 quartz shear vein is parallel with the fault. Site 24. **(B)** Outcrop view highlighting the abundance of D3 normal and strike-slip faults that cut the surrounding fabrics. Site 29. **(C)** D3 shear vein along a strike-slip fault in the Constitution terrane sandstone. Site 23. **(D)** Brittle D3 normal faults cutting S1 foliation in Deadman Bay terrane ribbon chert. Notebook for scale. Site 48.

Figure 12. Equal area stereonet plots of D3 faults including poles to planes, slip directions of the hanging wall, and compression and tension strain axes from FaultKinWin (Allmendinger, 2016) analysis. Symbols: squares = poles to fault plane, solid dots = compression axes, open dots = tension axes, and dots with arrows = lineations and direction of slip. **(A)** Poles to normal fault planes. **(B)** Normal fault planes with slip directions. **(C)** Compression and tension strain axes for normal faults. 1% area contour plot of tension axes for normal faults. Contour interval is 2%. **(D)** Strike-slip fault planes with slip directions. **(E)** Compression and tension strain axes for strike-slip faults. **(F)** Strike-slip fault planes. Left-lateral faults shown as black and right-lateral faults shown as red. **(G)** Thrust fault planes with slip directions. **(H)** Compression and tension strain axes for thrust faults.

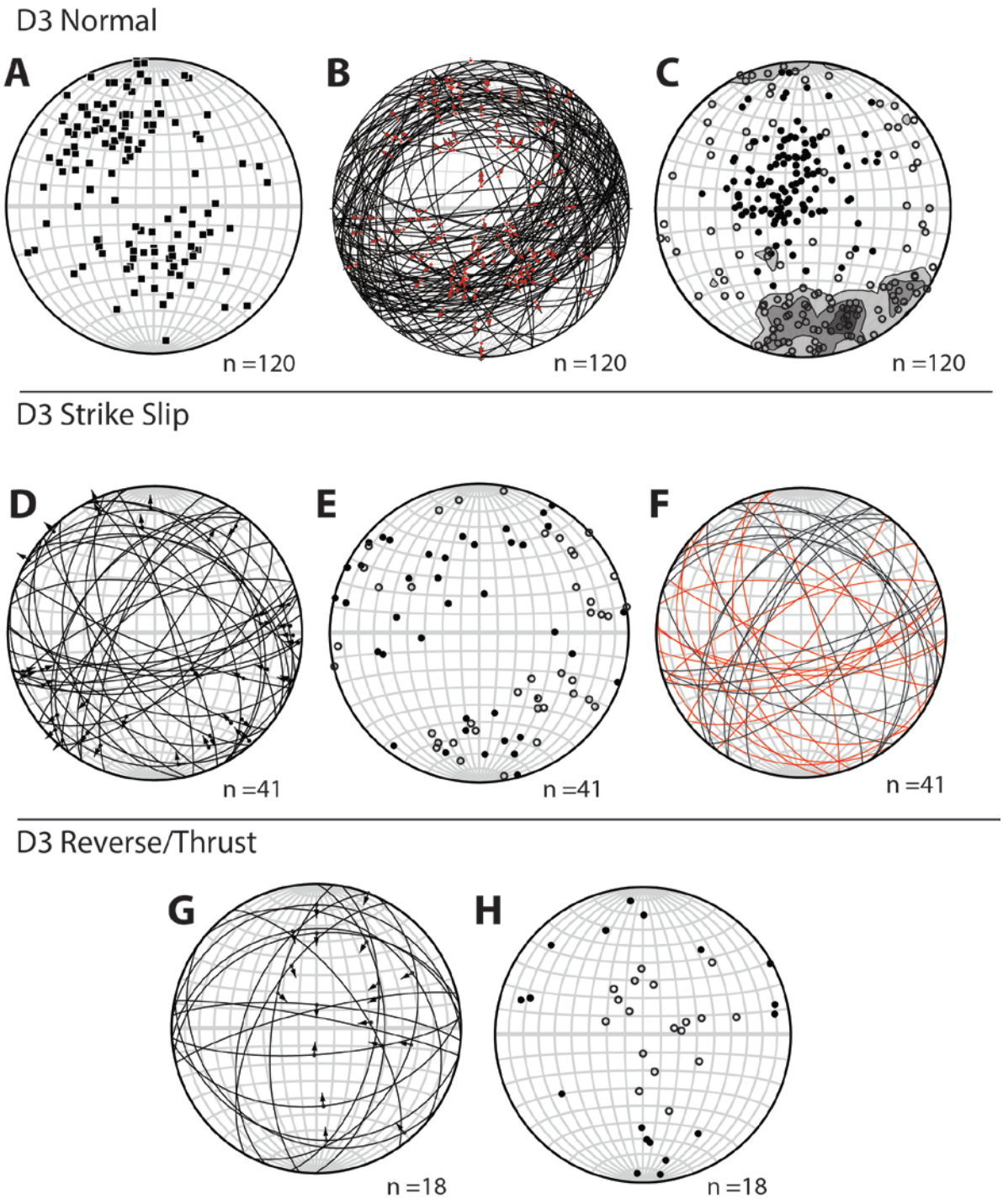

Caption on previous page.

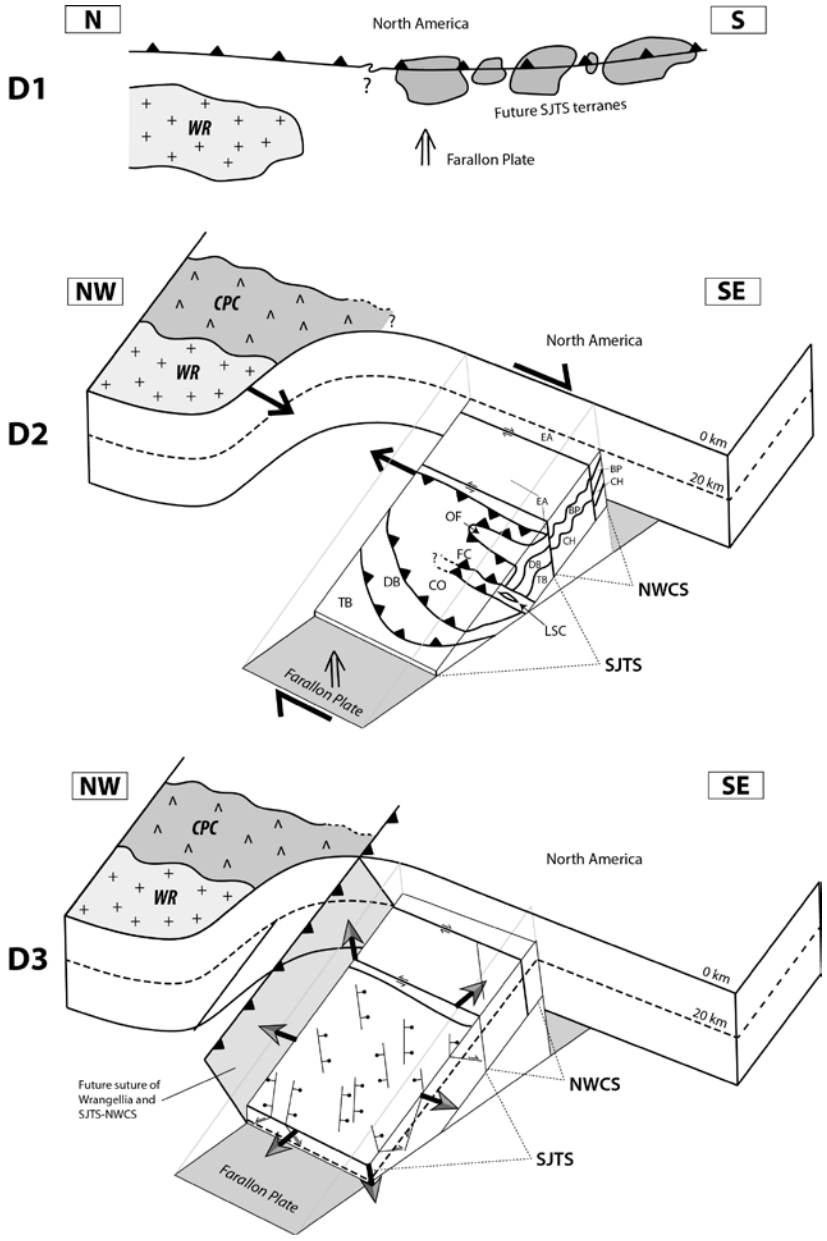

Figure 13. Schematic diagrams depicting the interpreted tectonic evolution of the SJTS-NWCS. **(D1)** Terranes accrete separately along the North American margin as they enter into an accretionary wedge environment. Wrangellia is nearing collision with the continent somewhere north of the SJTS terranes. **(D2)** Oblique subduction is initiated and terranes are thrust and assembled on top of one another over the already accreted Wrangellia. Abbreviations as in figure 1. BP – Bell Pass Mélange terrane; EA – Easton. **(D3)** D3 brittle structures accommodate horizontal extension with predominant margin-parallel extension. The future (unidentified) suture of the SJTS-NWCS terranes and Wrangellia is shown in gray. Schematics are modeled after Brown (1987) (D1) and Schermer et al. (2007) (D2 and D3).

Chapter 2: Fluid Inclusion Results

INTRODUCTION

Understanding P-T conditions during deformation of accreted terranes is important for understanding the pathways rocks took during accretion and emplacement. Pressure and temperature conditions in the SJTS have been constrained by the presence of HP-LT minerals aragonite, prehnite, and lawsonite in veins and fault rock (Glassley et al., 1976; Brandon et al., 1988, 1993, Maekawa and Brown, 1991; Schermer et al., 2007). As discussed above, these constraints broadly indicate relatively stable metamorphic conditions of no more than ~200˚C at ≥5.5 kb during all (D1-D3) deformation events. In attempt to provide tighter constraints on the P-T conditions of each deformation phase, fluid inclusions within quartz and calcite veins from faults of known kinematics were analyzed. Pairing fluid inclusion results with metamorphic mineral assemblages can provide insight into how deformation relates to fluid flow and depth in an accretionary wedge.

Physical and chemical conditions of fluids entrapped within a mineral at the time of mineral formation can be determined with fluid inclusion microthermometry (Roedder, 1984; Goldstein and Reynolds, 1994). If the morphology of fluid inclusions suggests that the volume of the inclusions within an assemblage has not changed since mineral formation, then microthermometry can be used to determine the minimum temperatures at the time of the deformation that produced the vein. After entrapment, the drop in temperature and pressure during exhumation cause the formation of a gas phase within fluid inclusions. Microthermometry provides a homogenization temperature (Th) that represents the minimum temperature required for the inclusion to homogenize back into an all-fluid state as it was during entrapment. Additionally, after freezing the inclusions, the final melting temperature

of ice (Tm) allows determination of the fluid's composition. Combining Th and Tm produces an isochore (line of constant volume) on a P-T graph representing the possible pressures and temperatures of mineral formation. Th values only provide a minimum estimate of entrapment temperature and require a pressure correction to estimate actual entrapment temperatures. If pressure estimations from metamorphic minerals are available (e.g. aragonite, lawsonite, or prehnite), actual entrapment temperatures can be constrained, and vice versa.

SAMPLE PREPARATION

Coarse-grained quartz and carbonate veins associated with the D1 and D3 events were sampled for fluid inclusion microthermometry (Figs. 14, 15). Although other quartz and carbonate veins in the SJTS contain additional minerals such as lawsonite and prehnite, the sampled veins did not. Two of the samples analyzed using fluid inclusion microthermometry were confirmed to be aragonite using X-ray diffraction analysis. To identify optimum samples to be professionally polished, ~120μm thick quick-plates of 42 samples were ground to 600 grit on both sides and observed using water and a cover slip to improve clarity. Most samples lacked identifiable primary inclusions and were clouded by an abundance of inclusions too small to analyze. Fourteen samples with the best evidence for growth zones and their optical clarity (3 from D1 and 11 from D3) were doubly polished.

Quartz-rich samples proved more useful than calcite for identifying primary inclusions, having 1) more inclusions, 2) better optical clarity for analyzing small inclusions, and 3) and easily identifiable fractures and secondary inclusion trails. Carbonate samples were rarely chosen for analysis. Cleavage planes in carbonate crystals are weak, and

assemblages along cleavage planes were avoided due to their high potential for fracturing and allowing entrapment of secondary inclusions during later geologic deformation (Fig. 16A). Additionally, primary inclusions in carbonate samples are difficult to identify due to the high density of secondary fractures. Quartz samples possess abundant scattered inclusions and rare growth zones characteristic of primary inclusions (Figs. 16B-D). Assemblages of primary inclusions were identified as being parallel to grain boundaries and isolated from potential fractures (Roedder, 1984). Fifteen total assemblages were deemed primary, with at least one assemblage in each of the 14 samples.

FLUID INCLUSION MICROTHERMOMETRY

Microthermometry was conducted at Western Washington University under the supervision of Dr. Pete Stelling using an Olympus BX53 petrographic microscope and 40x objective, Linkam THMSG600 temperature-controlled geologic stage, and Linksys32 temperature control and video capture software. The eutectic temperature (Te) and the final ice-melting temperature of ice (Tm) for each inclusion were measured prior to heating runs in attempt to avoid inclusion decrepitation (Roedder, 1984). Freezing was characterized by the "jerk" of the vapor phase bubble, slight darkening of the inclusions, or sudden disappearance of the vapor phase during ice formation. Aqueous inclusions were cooled to -60˚C during repeated cooling runs. Th values were measured using the bracketing technique described in detail by Goldstein and Reynolds (1994). Heating rates of 0.25-0.5 ˚C/min were chosen when nearing phase transitions. Tm was generally observed as a sudden jerk followed by a lack of observable bubble deformation, or as the vapor phase suddenly re-nucleated with no

noticeable post-nucleation bubble deformation. Salinity (weight % NaCl) was calculated using equations from Bodnar (1993).

RESULTS

Assemblages from both D1 and D3 vein samples have similar sizes, morphologies, and general fluid compositions. Inclusions are rounded to sub-rounded, averaging 3-5 um in the longest dimension (Fig. 16). All analyzed assemblages are two-phase (vapor-fluid) inclusions at room temperature with vapor volume % varying between 15 - 40%, averaging 25%. First melting (Te) values averaging near -21.1˚C indicate a H_2O + NaCl fluid system.

Reliable data were difficult to obtain due to 1) vapor phases disappearing upon freezing cycles and failing to reappear when heating, 2) presence of accidentals (solids entrapped during mineral formation), 3) and a lack of observable bubble deformation during the melting. Small inclusion sizes and poor sample clarity amplified the latter problem. Analysis of four of the assemblages produced datasets large enough to allow for interpretation of fluid conditions (Fig. 17; Table 2); quartz samples ORC-10-6-15-1A and B from D1, and quartz samples ORC-7-23-15-1B and ORC-7-19-15-4C from D3 (normal faults). Tm values for D1 assemblages varied from -4.3 to 1˚C, averaging -1.9˚C (Fig. 15; Table 2). Th values for D1 assemblages are scattered between 157-248˚C (Fig. 17; Table 2). Tm values for D3 assemblages had two populations; in sample ORC-7-23-15-1B values ranged between -3.7 to -2.2˚C averaging -2.8˚C, while sample ORC-7-19-15-4C values ranged between -1.8 to 1.7˚C, averaging -0.7˚C (Fig. 17; Table 2). Th values for D3 assemblages also show two populations; sample ORC-7-23-15-1B shows scatter between 212-299˚C, while ORC-7-19-15-4C scatters between 168-230˚C (Fig. 17; Table 2).

INTERPRETATION

Due to the wide variability in Tm and Th data for D1 and D3 assemblages, the inclusions are believed to have reequilibrated (change in volume and/or composition) and are deemed untrustworthy for estimating P-T conditions. Inclusions may have reequilibrated by a combination of (1) dislocation creep processes, (2) unstable crack growth during inclusion decrepitation, or (3) undetected necking down after a phase change (Goldstein and Reynolds, 1994). A component of dislocation creep is evident as weak undulatory extinction in quartz grains (Fig. 16B). Kerrich (1976) states that even small amounts of strain can cause minor intracrystalline leakage of fluids yielding abnormally high temperature estimates. Relatively consistent gas-to-liquid ratios, lack of single-phase (all liquid) inclusions, and generally rounded morphology suggest necking was not the primary factor in causing Tm and Th variability. A more likely cause for reequilibration is a combination of volume changes by cracking (or stretching) and fluid leakage/refilling due to dislocation creep and/or fracturing (Goldstein and Reynolds, 1994). Positive Tm values in some samples may indicate metastability of inclusions as the vapor phase fails to re-nucleate until positive temperature values as a result of negative pressures caused by the disappearance of the vapor phase during freezing tests (Roedder, 1967). These positive values may also suggest the presence of other fluid components having positive melting temperatures, such as CO_2 clathrates or other gas hydrates (Bozzo, 1975; Collins, 1979; Goldstein and Reynolds, 1994). Though the results do not allow an accurate interpretation of the exact fluid composition, they do suggest fluid with salinities <7 wt. %.

A preliminary fluid inclusion investigation by Gillaspy (2004) in the SJTS suggested similar findings of reequilibration after entrapment for assemblages in veins similar to D3 of this study. Gillaspy (2004) found similarly sized, two-phase H_2O + NaCl aqueous inclusions with salinities of ~0.5 wt. % and Th values ranging from 177 to 206˚C. Th values represent minimum entrapment temperatures and are often lower than temperatures required by mineralogical constraints, however. In both Gillaspy's (2004) data and data presented here, most of the minimum entrapment temperatures are too high for rocks preserving aragonite (Fig. 18; Carlson and Rosenfeld, 1981). Using isochores from Gillaspy (2004) and those calculated from data above (assuming inclusions are still in equilibrium), pressures as low as <0.25 kbar are required to agree with the interpreted maximum temperature of 200˚C (Fig. 18). Aragonite does not form in equilibrium at such low pressures, as pressures of ~5.5 kbar (Boettcher and Wyllie, 1968; Crawford and Hoersch, 1972) and 6.5 kbar (Redfern et al., 1989) are estimated for aragonite. These calculated low pressures can be explained by stretching of the fluid inclusions due to deformation during rising temperatures after fluid entrapment.

Further fluid inclusion work in the SJTS may be successful if veins are found with more conclusive evidence for primary inclusions, and if larger inclusions can be found or can be analyzed with higher magnification objectives (>40x). Additionally, cathodoluminescence of veins could be used to look for textural evidence of multiple generations of growth at different times.

TABLES

TABLE 2. MICROTHERMOMETRY DATA FOR FLUID INCLUSION ANALYSIS

Sample†	Inclusion	% Gas *	Tm (˚C)	Wt. % Salinity	Th (˚C)
ORC-10-6-15-1A	1	35	-0.7	1.2	197
Quartz	2	30	-2.1	3.5	202.5
	3	35	-1.2	2.1	202.2
	4	25	-2	3.4	207
	5	25	-2.5	4.2	216
	6	25	-2.3	3.9	248
	7	20	-3.8	6.2	227
	8	25	-1.7	2.9	217
	9	20	0	0.0	157
	10	25	-2.4	4.0	237
	11	30	-2	3.4	200
	12	35	-2	3.4	247
ORC-10-6-15-1B	1	25	-4.3	6.9	218
Quartz	2	30	-3.1	5.1	233
	3	20	-2.4	4.0	-
	4	30	-2.2	3.7	192
	5	35	-1.9	3.2	212.5
	6	30	-1.5	2.6	197.5
	7	20	0.3	-	182.5
	8	30	-1.7	2.9	227.5
	9	30	-1.8	3.1	197.5
	10	20	-3.2	5.3	197.5
	11	40	-3.6	5.9	182.5
	12	30	-1.2	2.1	182.5
	13	25	1	-	177.5
ORC-7-19-15-4C	1	15	-0.4	0.7	172.5
Quartz	2	20	-1.4	2.4	180
	3	20	-0.6	1.1	168
	4	20	2.5	-	165
	5	20	1.7	-	180
	6	30	-1.1	1.9	173
	7	20	1	-	180
	8	20	-1.3	2.2	226
	9	20	-0.6	1.1	-
	10	25	-	0.0	-
	11	20	-1.8	3.1	181
	12	30	-1.2	2.1	230
	13	25	-0.6	1.1	-
	14	15	-1.1	1.9	174
	15	20	-1.1	1.9	201
	16	25	-1.3	2.2	224

TABLE 2. Cont'd

Sample†	Inclusion	% Gas *	Tm (˚C)	Wt. % Salinity	Th (˚C)
ORC-7-8-15-4D	1	20	-0.1	0.2	-
Quartz	2	25	0.1	-	-
	3	20	2.3	-	-
	4	20	-2.3	3.9	-
	5	20	-1.1	1.9	-
	6	20	-1.4	2.4	-
	7	25	-0.9	1.6	-
	8	25	-	-	-
	9	30	-0.8	1.4	-
	10	25	-0.9	1.6	-
	11	15	-0.8	1.4	-
	12	30	-0.9	1.6	-
	13	30	0.5	-	-
	14	30	-1.7	2.9	-
	15	20	-0.9	1.6	-
	16	30	-1.2	2.1	-
ORC-7-22-15-3D	1	25	-	-	427
Quartz	2	30	-	-	417
	3	20	-	-	432
	4	25	-	-	-
	5	25	-	-	456
	6	30	-	-	-
	7	35	-	-	463
	8	30	-	-	-
	9	30	-	-	422
	10	30	-	-	-
ORC-7-22-15-3E	1	30	-	-	49.3
Quartz	2	50	-2.7	4.5	363
	3	25	-4.5	7.2	-
	4	25	-	-	-

TABLE 2. Cont'd

Sample†	Inclusion	% Gas *	Tm (˚C)	Wt. % Salinity	Th (˚C)
ORC-7-23-15-1B	1	25	-2.5	4.2	230
Quartz	2	35	-2.2	3.7	250
	3	30	-2.5	4.2	245
	4	25	-3.4	5.6	265
	5	20	-2.9	4.8	274
	6	40	-3.4	5.6	299
	7	35	-2.8	4.6	281
	8	30	-2.4	4.0	241
	9	25	-2.6	4.3	215
	10	20	-2.2	3.7	212
	11	40	-3.7	6.0	253
ORC-7-29-15-4A	1	30	-	-	242.5
Quartz	2	30	-	-	-
	3	30	-	-	208
	4	30	-	-	-
	5	30	-	-	-
	6	30	-	-	180
	7	30	-	-	239
	8	30	-	-	-
	9	30	-	-	-
	10	30	-	-	227
	11	30	-	-	230
	12	30	-	-	218
	13	30	-	-	-
ORC-7-29-15-4C	1	40	-1	1.7	228.3
Quartz	2	25	-	0.0	-
	3	40	-1.2	2.1	196.7
	4	35	1.6	-	232
	5	25	0	0.0	228.5
	6	30	2	-	205
	7	30	2.3	-	220

TABLE 1. Cont'd

Sample†	Inclusion	% Gas *	Tm (˚C)	Wt. % Salinity	Th (˚C)
ORC-9-3-15-1F	1	10	-	-	177
Carbonate	2	25	-	-	177
	3	25	-1.6	2.7	165
	4	25	-	0.0	-
	5	30	-2	3.4	206
	6	25	0.4	-	134
ORC-9-3-15-1F-2	**1**	30	1.9	-	263
Carbonate	2	30	2.3	-	267
	3	30	0.5	-	209
	4	30	2.1	-	251
	5	30	-1.1	1.9	242
	6	30	3	-	175
	7	20	4.5	-	180
	8	30	0.5	-	-
	9	30	0.5	-	-
	10	30	2.5	-	-
	11	30	4.4	-	188
	12	30	-	-	263
	13	30	0.1	-	-
	14	20	-0.8	1.4	192
	15	30	-1.1	1.9	192
	16	30	-1.1	1.9	162
	17	30	2.4	-	-
	18	30	3	-	-
	23	30	-1.2	2.1	170
	25	30	-1.1	1.9	165

† Sample numbers listed for 12 of the 15 samples analyzed. Three samples produced no data. Samples ending in A, B, C, etc. denote separate pieces of one polished thick section. Samples ORC-9-3-15F and F-2 are two separate assemblages within one piece of the polished thick section.
Sample locations listed in table A1.

* Estmated volume % of the inclusion occupied by vapor.

" - " Represents lack of Th or Tm data for various reasons stated in text, or impossible salinity values correlating to positive Tm values (Bodnar, 1993).

FIGURES

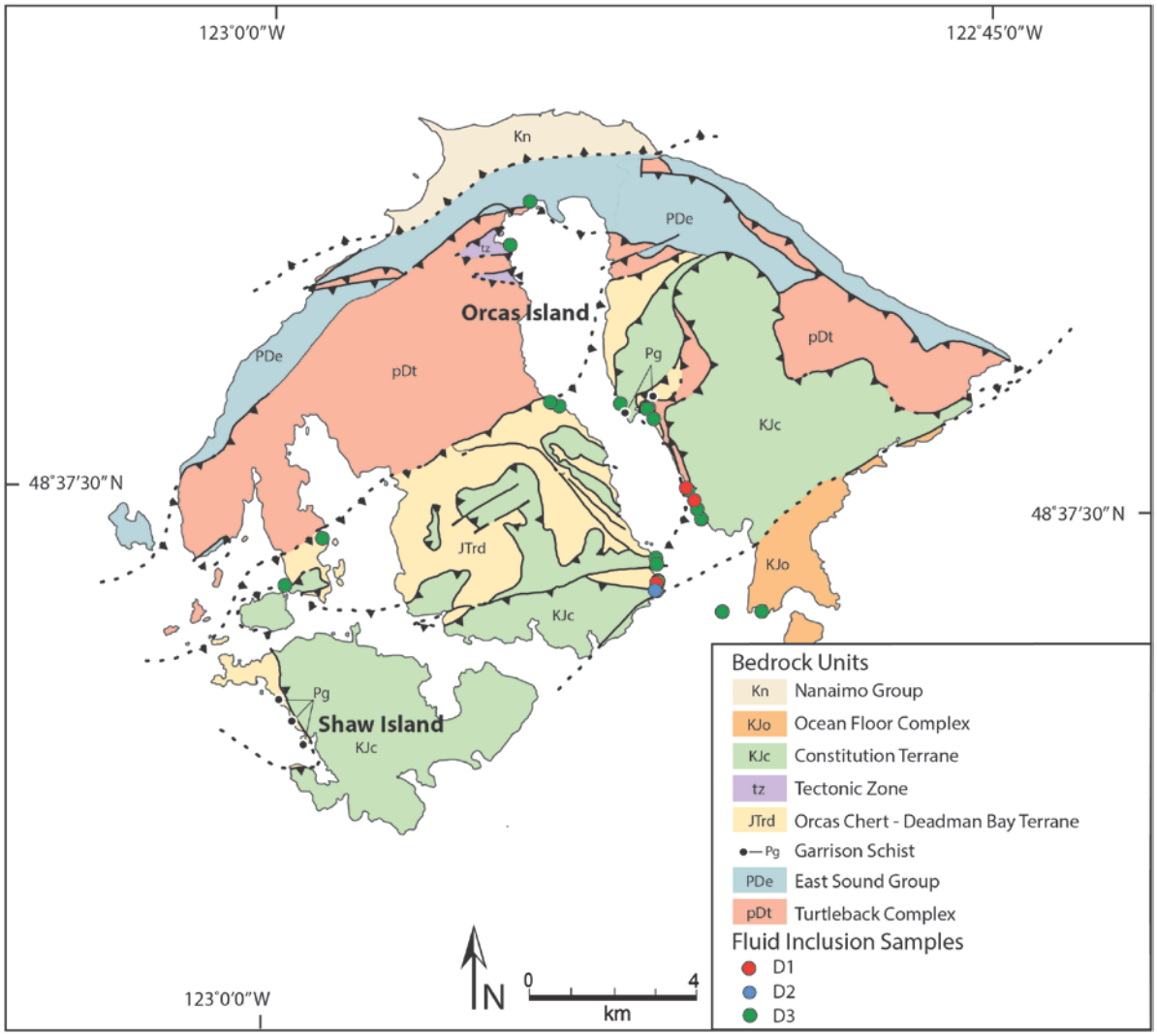

Figure 14. Geologic map of Orcas and Shaw Islands showing the locations of veins sampled for fluid inclusion investigations. Sample numbers located in table A1.

Figure 15. Outcrop photos of veins sampled for fluid inclusion work. **(A)** Carbonate D1 vein cut by a D2 shear zone. Sample 9-7-15-6. Site 26. **(B)** Carbonate vein along a D3 dextral strike-slip fault. Sample 7-18-15-1. Site 23. **(C)** Quartz vein along a D3 normal fault. Sample ORC-7-19-15-4. Site 24.

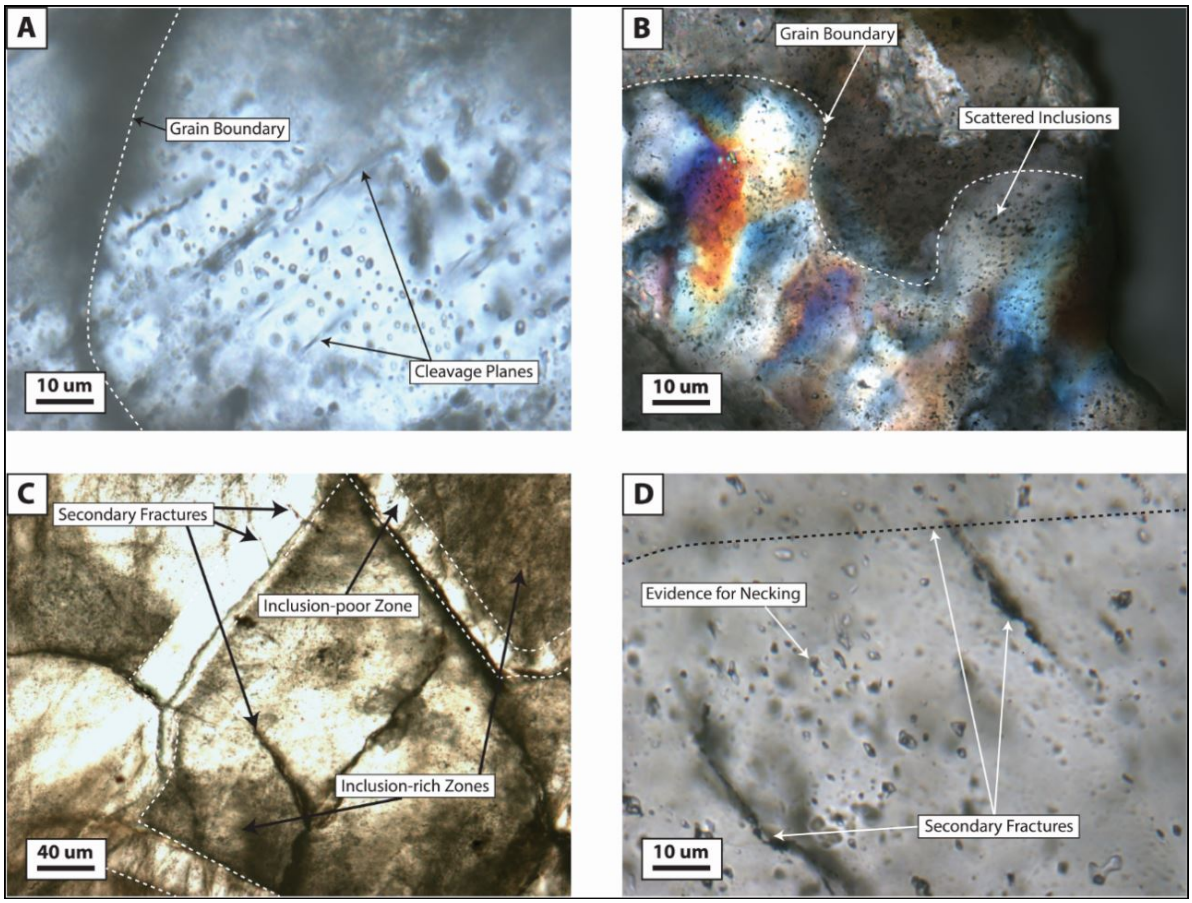

Figure 16. Photomicrographs of aqueous inclusions in thick sections of quartz and carbonate vein samples. **(A)** D3 carbonate vein (sample ORC-9-3-15-1) with primary inclusions amongst abundant cleavage planes. Photo taken in plane light. **(B)** D1 quartz vein (sample ORC-10-6-15-1B) with undulatory extinction and abundant scattered aqueous inclusions. Photo taken with crossed polars. **(C)** D3 quartz vein (sample ORC-9-3-15-1) showing an abundance of scattered inclusions. Dashed lines indicate a growth zone lacking inclusions. Fractures (some with secondary inclusions along them) cut these zones. Photo taken in plane light. **(D)** Primary aqueous inclusions in a D3 quartz vein (sample 7-23-15-1B) with two-phase primary inclusions. Note both the small nature of inclusions and abundance of fractures. Evidence for a necked inclusion suggests that necking may have taken place in other inclusions. Photo taken in plane light.

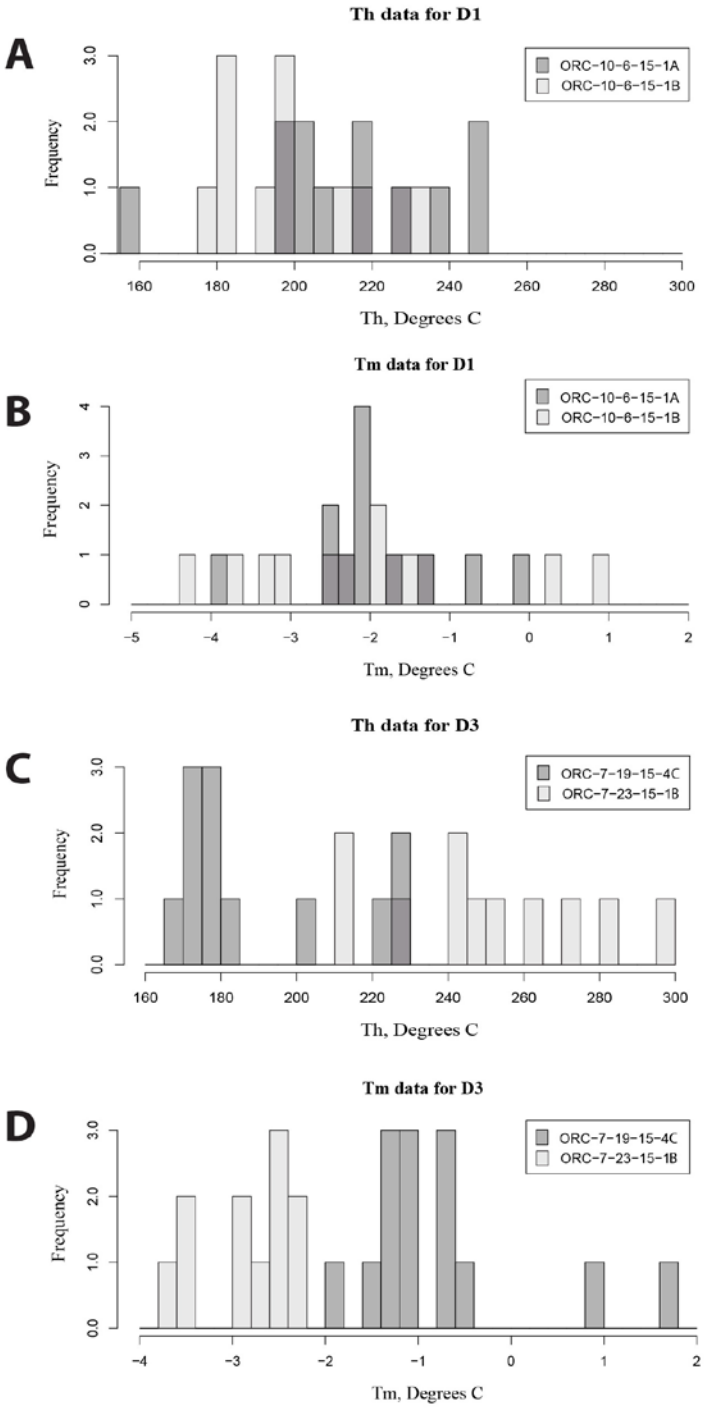

Figure 17. Histograms of microthermometric data for fluid assemblages in D1 and D3 quartz veins. Only samples that produced large datasets are included for reasons discussed in the text. **(A)** Th data for D1 samples. **(B)** Tm data for D1 samples. **(C)** Th data for D3 samples. **(D)** Tm data for D3 samples.

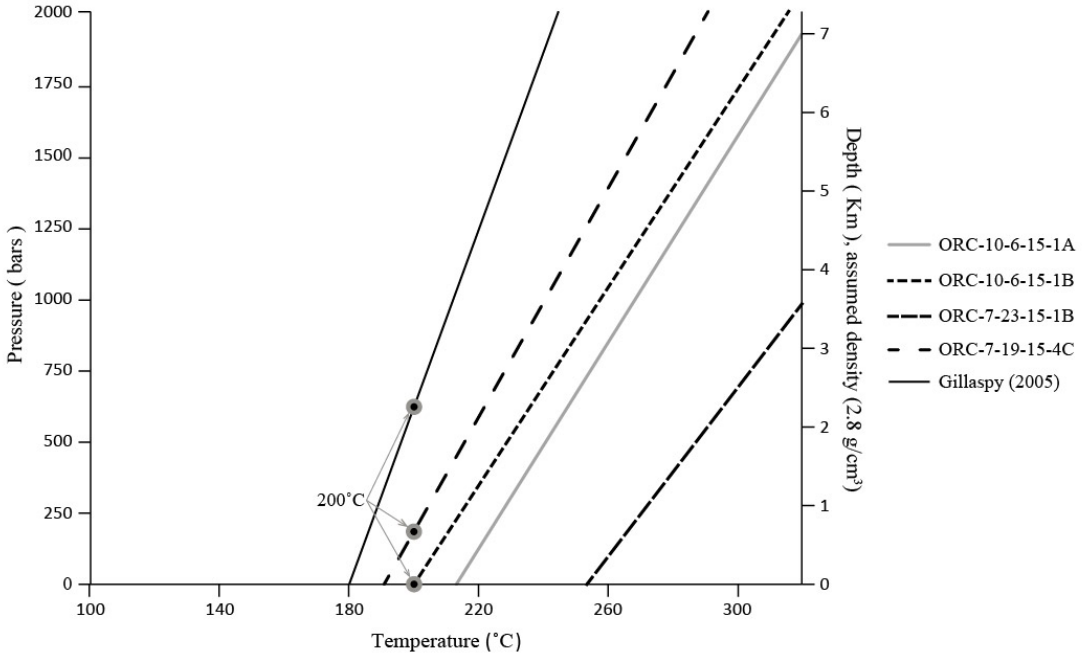

Figure 18. Isochores calculated using microthermometry data (Table A1) and equations derived by Bodnar (1993) for H_2O + NaCl fluid systems. Calculations assume inclusions have not reequilibrated. Labels at 200˚C highlight the pressures along each isochore that would be required to reach the interpreted maximum temperature indicated by the preservation of aragonite in the SJTS.

REFERENCES CITED

Allmendinger, R.W., 2016, StereoWin v. 9.5.0, FaultKinWin v. 7.4.1, http://www.geo.cornell.edu/geology/faculty/RWA/programs/ (January, 2016).

Avé Lallemant, H.G., and Guth, L.R., 1990, Role of extensional tectonics in exhumation of eclogites and blueschists in an oblique subduction setting: Geology, v. 18, p. 950 – 953.

Avé Lallemant, H.G., and Oldow, J.S., 2000, Active displacement partitioning and arc-parallel extension of the Aleutian volcanic arc based on Global Positioning System geodesy and kinematic analysis: Geology, v. 28, p. 739 – 742.

Beck Jr. M.E., Burmester, R.F., Engebretson, D.C, and Schoonover, R., 1981, Northward translation of Mesozoic batholiths western North America: Paleomagnetic evidence and tectonic significance: Geofisica Internacional, v. 20, p. 143 – 162.

Belanger, T.T., 2008, Structural geology of the central San Juan Islands, northwest Washington [M.S. Thesis], Western Washington University, Bellingham, WA, 145 p.

Bergh, S.G., 2002, Linked thrust and strike-slip faulting during Late Cretaceous terrane accretion in the San Juan thrust system, Northwest Cascade orogen, Washington: Geological Society of America Bulletin, v. 114, p. 934 – 949.

Berthé, D., Choukroune, P., and Jégouzo, P., 1979, Orthogneiss, mylonite and non coaxial deformation of granites: the example of the South Armorican Shear Zone: Journal of Structural Geology, v. 1, p.31 – 42.

Bodnar, R.J., 1993, Revised equation and table for determining the freezing point depression of H_2O-NaCl solutions, Geochimica et Cosmochimica Acta, v. 57, p. 683 – 684.

Bozzo, A.T., Chen, H-S., Kass, J.R., and Barduhn, A.J., 1975, The properties of hydrates of chlorine and carbon dioxide, Desalination, v. 16, p. 303 – 320.

Boettcher, A.L., and Wyllie, P.J., 1968, The Calcite-Aragonite Transition Measured in the System CaO-CO_2-H_2O: The Journal of Geology, v. 76, p. 314 – 330.

Bott, M.H.P., 1959, The mechanics of oblique slip faulting: Geological Magazine, v. 96, p. 109 – 117.

Brandon, M.T., and Cowan, D.S., 1985, The Late Cretaceous San Juan Island – Northwestern Cascades thrust system: Geological Society of America Abstracts with Programs, v. 17, p. 343.

Brandon, M.T., Cowan, D.S., Feehan, J.G., 1993, Kinematic analysis of the San Juan thrust system, Washington: Discussion and reply: Geological Society of America Bulletin, v. 105, p. 839 – 844.

Brandon, M.T., Cowan, D.S., Feehan, J.G., 1994, Fault-zone structures and solution-mass-transfer cleavage in Late Cretaceous nappes, San Juan Islands, Washington, *in* Swanson, D.A., and Haugerud, R.A., eds., Geologic Field Trips in the Pacific Northwest: Geological Society of America Annual Meeting, Field Trip guidebook, p. 2L-1 – 2L-19.

Brandon, M.T., Cowan, D.S., and Vance, J.A., 1988, The Late Cretaceous San Juan thrust system, San Juan Islands, Washington: Geological Society of America Special Paper 221, 81 p.

Brown, E.H., 1987, Structural geology and accretionary history of the Northwest Cascades system, Washington and British Columbia: Geological Society of America Bulletin, v. 99, p. 201 – 214.

Brown, E.H., 2012, Obducted nappe sequence in the San Juan Islands – northwest Cascades thrust system, Washington and British Columbia: Canadian Journal of Earth Science, v. 49, p. 796 – 817.

Brown, E.H., Lapen, T.J., Leckie, R.M., Silva, I.P., Verga, D., and Singer, B.S., 2005, Revised ages of blueschist metamorphism and the youngest pre-thrusting rocks in the San Juan Islands, Washington: Canadian Journal of Earth Sciences, v. 42, p. 1389 – 1400.

Brown, E.H., and Gehrels, G.E., 2007, Detrital zircon constraints on ages and affinities and timing of orogenic events in the San Juan Islands and North Cascades, Washington: Canadian Journal of Earth Sciences, v. 44, p. 1375 – 1396.

Burmester, R.F., Blake, M.C.J., and Engebretson, D.C., 2000, Remagnetization during Cretaceous normal superchron in eastern San Juan Islands, WA: Implications for tectonic history: Tectonophysics, v. 326, p. 73 – 92.

Carlson, W.D., and Rosenfeld, J.L., 1981, Optical determination of topotactic aragonite-calcite growth kinetics: Metamorphic implications: The Journal of Geology, v. 89, p. 615 – 638.

Carmignani, L., Kligfield, R., 1990, Crustal extension in the northern Apennines: transition from compression to extension in the Alpi Apuane core complex: Tectonics, v. 9, p. 1275 – 1303.

Collins, P.L., 1979, Gas hydrates in CO_2-bearing fluid inclusions and the use of freezing data

for estimation of salinity, Economic Geology, v. 74, p. 1435 – 1444.

Cowan, D.S. and Brandon, M.T., 1994, A symmetry-based method for kinematic analysis of large-slip brittle fault zones: American Journal of Science, v. 294, p. 257 – 306.

Cowan, D.S., and Miller, R.B., 1981, Deformation styles in two Mesozoic fault zones, western Washington, USA. *in* Thrust and Nappe tectonics. *Edited by* K.R. McClay, and N.J Price. The Geological Society of London Special Publication 9, pp. 483–490

Crawford, W.A., and Hoersch, A.L., 1972, Calcite-aragonite equilibrium from 50 °C to 150°C: American Mineralogists, v. 57, p. 995 – 998.

Danner, W.R., 1966, Limestone resources of western Washington, with a section on the Lime Mountain deposit by G.W. Thorsen: Washington Division of Mines and Geology Bulletin, v. 52, 474 p.

Davis, D.M., 1996, Accretionary mechanisms with properties that vary in space and time: Subduction: Top to Bottom, Geophysical Monograph 96, p. 39 – 48.

Davis, D.M, Suppe, J., Dahlen, F.A., 1983, Mechanics of fold-and-thrust belts and accretionary wedges: Journal of Geophysical Research, v. 88, p. 1153 – 1172.

Doblas, M., 1998, Slickenside kinematic indicators: Tectonophysics, v. 295, p. 187 – 197.

Dresan, G., 1991, Stress distribution and the orientation of Riedel shears: Tectonophysics, v. 188, p. 239 – 247.

Durney, D.W., and Ramsay, J.G., 1973, Incremental strains measured by syntectonic crystal growth: Gravity and Tectonics, v. 1, p. 67 – 96.

Feehan, J.G., Brandon, M.T., 1999, Contribution of ductile flow to exhumation of low-temperature, high-pressure metamorphic rocks: San Juan-Cascades nappes, NW Washington State: Journal of Geophysical Research, v. 104, p. 10,883 – 10,902.

Frey, M., De Capitani, C., and Liou, J.G., 1991, A new petrogenetic grid for low-grade metabasites: Journal of Metamorphic Geology, v. 9, p. 497 – 509.

Friedman, R.M., and Armstrong, R.L., 1995, Jurassic and Cretaceous geochronology of the southern Coast Belt, British Columbia, 49˚ to 51˚N: Geological Society of America Special Paper 299, p. 95 – 139.

Gillaspy, J.R., 2004, Brittle deformation in an ancient accretionary prism setting: Lopez Structural Complex, San Juan Islands, NW Washington [M.S. thesis]: Western Washington University, 134 p.

Glassley, W.E., Whetten, J.T., Cowan, D.S., and Vance, J.A., 1976, Significance of coexisting lawsonite, prehnite, and aragonite in the San Juan Islands, Washington: Geology, v. 4, p. 301 – 302.

Goldstein, R.H., Reynolds, J.T., 1994, Systematics of fluid inclusions in diagenetic minerals: Society for Sedimentary Geology, SEPM Short Course 31, 199 p.

Hansen, E., 1971, Strain Facies: New York, Springer-Verlag, 207 p.

Hayman, N.W., Byrne, T.B., McNeill, L.C., Kanagawa, K., Kanamatsu, T., Browne, C.M., Schleicher, A.M., and Huftile, G.J., 2012, Structural evolution of an inner accretionary wedge and forearc basin initiation, Nankai margin, Japan, Earth and Planetary Science Letters, v. 353, p. 163 – 172.

Housen, B.A., Beck, M.E., Jr. Burmester, R.F., Fawcett, T., Petro, G., Sargent, R., Addis, K., Curtis, K., Ladd, J., Liner, N., Molitor, B., Montgomery, T., Matnatt, I., Palmer, B., Tucker, D., and White, I., 2003, Paleomagnetism of the Mt. Stuart Batholith revisited again; what has been learned since 1972?: American Journal of Science, v. 203, p. 263 – 299.

Irving, E., 1985, Whence British Columbia?: Nature, v. 314, p. 673–674.

Joint Committee on Powder Diffraction Standards, 1980, Mineral Powder diffraction files – data book: JCPDS International Centre for Diffraction Data, Swarthmore, Pennsylvania. 1168 p.

Kerrich, R., 1976, Some effects of tectonic recrystallization on fluid inclusion in vein quartz: Contributions to Mineralogy and Petrology, v. 59, p. 195 – 202.

Kuramoto, S., and Konishi, K., 1989, The southwest Ryukyu arc is a migrating microplate (forearc sliver): Tectonophysics, v. 163, p. 75 – 91.

Maekawa, H., Brown, E.H., 1991, Kinematic analysis of the San Juan thrust system, Washington: Geological Society of America Bulletin, v. 103, p. 1007 – 1016.

Maekawa, H., Brown, E.H., 1993, Kinematic analysis of the San Juan Thrust System, Washington: Reply: Geological Society of America Bulletin, v. 105, p. 839 – 844.

Maerten, L., Gillespie, P., and Pollard, D.D., 2002, Effects of local stress perturbation on secondary fault development: Journal of Structural Geology, v. 24, p. 145 – 153.

Marrett, R.A., and Allmendinger, R. W., 1990, Kinematic analysis of fault-slip data: Journal of Structural Geology, v. 12, p. 973 – 986.

McCaffrey, R., 1992, Oblique plate convergence, slip vectors, and forearc deformation: Journal of Geophysical Research, v. 97, p. 8905 – 8915.

McCaffrey, R., 1996, Estimates of modern arc-parallel strain rates in forearcs: Geology, v. 24 , p. 27 – 30.

McGroder, M.F., 1991, Reconciliation of two-sided thrusting, burial metamorphism, and diachronous uplift in the Cascades of Washington and British Columbia: Geological Society of America Bulletin, v. 103, p. 189 – 209.

Meneghini, F., Marroni, M., Moore, J.C., Pandolfi, L., Rowe, C.D., 2009, The processes of underthrusting and underplating in the geologic record; structural diversity between the Franciscan Complex (California), the Kodiak Complex (Alaska), and the Internal Ligurian Units (Italy): Geological Journal, v. 44, p. 126 – 152.

Misch, P. 1966. Tectonic evolution of the northern Cascades of Washington State - a west Cordilleran case history. *in* A Symposium on the Tectonic History and Mineral Deposits of the Western Cordillera in British Columbia and Neighboring Parts of the United States. *Edited by* H. C. Gunning. Canadian Institute of Mining and Metallurgy, Vancouver, B.C., 1964. Special Volume 8, p. 101 – 148.

Monger, J.W.H., and Ross, C.A., 1971, Distribution of fusulinaceans in the western Canadian Cordillera: Canadian Journal of Earth Sciences, v. 8, p. 259 – 278.

Moore, J.C., and Byrne, T., 1987, Thickening of fault zones: A mechanism of mélange formation in accreting sediments: Geology, v. 15, p. 1040 – 1043.

Petit, J.P., 1987, Criteria for sense of movement on fault surfaces in brittle rocks: Journal of Structural Geology, v. 9, p. 597 – 608.

Redfern, S.A.T., Salje, E., and Navrotsky, A., 1989, High-temperature enthalpy at the orientational order-disorder transition in calcite: Implications for the calcite/aragonite phase equilibrium: Contributions to Mineralogy and Petrology, v. 101, p. 479 – 484.

Roedder, E., 1967, Metastable superheated ice in liquid-water inclusions under high negative Pressure: Science, v. 155, p. 1413 – 1417.

Roedder, E., 1984, Fluid Inclusions: Mineralogical Society of America Reviews in Mineralogy, v. 12, 644 p.

Rubin, C.M., Saleeby, J.B., Cowan, D.S., Brandon, M.T., and McGroder, M.F., 1990, Regionally extensive mid-Cretaceous west-vergent thrust system in the northwestern Cordillera: Implications for continental margin tectonism: Geology, v. 18, p.276 – 280.

Sassi, W., and Faure, J.-L., 1997, Role of faults and layer interfaces on the spatial variation of stress regimes in basins: inferences from numerical modelling: Tectonophysics, v. 266, p. 101 – 119.

Schermer, E.R., Gillaspy, J.R., Lamb, R., 2007, Arc-parallel extension and fluid flow in an ancient accretionary wedge: The San Juan Islands, Washington: Geological Society of America Bulletin, v. 119, p. 753 – 767.

Shainin, V.E., 1950, Conjugate sets of en-echelon tension fractures in the Athens limestone: Geological Society of America Bulletin, v. 61, p. 509 – 517.

Simpson, C., De Paor, D.G., 1993, Strain and kinematic analysis in general shear zones: Journal of Structural Geology, v. 15, p. 1 – 20.

Stipp, M., Stunitz, H., Heilbronner, R., Schmid, S. M., 2002, The eastern Tonale fault zone: a 'natural laboratory' for crystal plastic deformation of quartz over a temperature range from 250 to 700 ˚C: Journal of Structural Geology, v. 24, p. 1861 – 1884.

Styron, R.H., Taylor, M.H., Murphy, M.A., 2011, Oblique convergence, arc-parallel extension, and the role of strike-slip faulting in the High Himalaya: Geosphere, v. 7, p. 582 – 596.

Surdam, R.C., 1973, Low-grade metamorphism of tuffaceous rocks in the Karmutsen Group, Vancouver Island, British Columbia; Geological Society of America Bulletin, v. 84, p. 1911 – 1922.

Twiss, R.J., Moores, E.M., 2007, Structural Geology (second edition): New York, W. H. Freeman and Company, 736 p.

Vance, J.A., 1975, Bedrock geology of San Juan County: *in* Geology and water resources of the San Juan Islands, San Juan County, Washington. *Edited by* R.H. Russell. Washington Department of Ecology. Water-Supply Bulletin 46, p. 3 – 19.

Wallace, R.E., 1951, Geometry of shearing stress and relation to faulting: Journal of Geology, v. 59, p. 118 – 130.

Wallis, S.R., Platt, J.P., Knott, S.D., 1993, Recognition of syn-convergent extension in accretionary wedges with examples from the Calabrian Arc and the Eastern Alps: American Journal of Science, v. 293, p. 463 – 495.

Ward, P.D., 1978, Revisions to the stratigraphy and biochronology of the Upper Cretaceous Nanaimo Group, British Columbia and Washington State: Canadian Journal of Earth Sciences, v. 15, p. 405–423.

Whitney, D.L., and McGroder, M.F., 1989, Cretaceous crustal section through the proposed

Insular-Intermontane suture, North Cascades, Washington: Geology, v. 17, p. 555 – 558.

Appendix

Table A2. Sample data from Orcas Island.

Structure*	Sample	Field Site # **	Map Reference # Σ	Easting Φ	Northing Φ	Analysis †	Aragonite	Calcite	Quartz	Prehnite	Chlorite
D1	ORC-9-7-15-6	26	1	510804	5386225	FI			x	x	x
	ORC-7-30-15-2	34	2	510112	5383778	XRD/FI		x	x		x
	ORC-10-6-15-1	58	3	511022	5385904	XRD/FI		x	x		
	ORC-10-6-15-2	58	4	511022	5385904	XRD	x	x	x		
	ORC-10-6-15-3	61	5	510544	5386414	XRD	x	x	x		
	ORC-9-6-15-1	40	6	506045	5392036						
D2	ORC-6-29-15-1	9	7	505868	5392624	XRD	x	x	x		
	ORC-7-1-15-1	15	8	506103	5392233						
	ORC-7-19-15-1	23	9	511170	5385469						
	ORC-8-1-15-7	37	10	510058	5387605						
	ORC-8-3-15-3	40	11	509890	5387956	XRD	x		x		
	ORC-9-7-15-1	49	12	500666	5383418						
	ORC-9-7-15-2	49	13	500666	5383418						
	ORC-9-7-15-3	49	14	500666	5383418						
	ORC-9-7-15-4	49	15	498378	5384062						
	ORC-9-7-15-7	26	16	510804	5386225						
D3 - Normal	ORC-6-26-15-2	4	17	512782	5383171						
	ORC-6-30-15-1	4	18	507482	5388218						
	ORC-6-30-15-2	13	19	509030	5388327						
	ORC-7-8-15-1	12	20	507252	5388307						
	ORC-7-8-15-2	12	21	507252	5388307						
	ORC-7-8-15-3	12	22	507252	5388307						
	ORC-7-8-15-4	12	23	507252	5388307	FI		x	x		
	ORC-7-9-15-1	20	24	509672	5388256						
	ORC-7-9-15-2	20	25	509703	5388244						
	ORC-7-9-15-3	20	26	509703	5388244						
	ORC-7-9-15-5	21	27	509747	5388250						
	ORC-7-19-15-2	23	28	511170	5385469	XRD		x	x		
	ORC-7-19-15-4	24	29	511060	5385718	FI		x	x		
	ORC-7-21-15-3	27	30	510814	5386189						
	ORC-7-22-15-3	30	31	510064	5384410	FI		x	x		
	ORC-7-23-15-1	31	32	510083	5384311	FI			x		
	ORC-7-29-15-2	33	33	510124	5383873						
	ORC-7-29-15-3	33	34	510124	5383873	XRD		x	x		
	ORC-7-30-15-1	34	35	510112	5383778						
	ORC-7-30-15-3	34	36	510112	5383778						
	ORC-7-31-15-5	35	37	510090	5383587	FI		x	x		x
	ORC-7-31-15-6	35	38	510079	5383575	XRD	x	x	x		
	ORC-8-2-15-1	39	39	506105	5392263	FI		x			
	ORC-8-2-15-2	39	40	506105	5392263						
	ORC-8-3-15-1	40	41	506046	5392078	XRD	x	x	x		
	ORC-8-3-15-4	40	42	506045	5392036	XRD/FI	x	x	x		
	ORC-8-3-15-6	40	43	506078	5392006						
	ORC-9-1-15-2	42	44	509024	5388328	XRD		x	x		
	ORC-9-3-15-1	48	45	501582	5384670	XRD/FI	x	x	x		
	ORC-9-3-15-2	48	46	501582	5384670	XRD		x	x		
	ORC-9-3-15-3	48	47	501582	5384670	XRD	x	x	x		
	ORC-9-4-15-2	50	48	500665	5383450						
	ORC-10-8-15-1	66	49	503615	5383088						

Table A2. Sample data from Orcas Island cont'd.

Structure*	Sample	Field Site # **	Map Reference # Σ	Easting ϕ	Northing ϕ	Analysis †	Aragonite	Calcite	Quartz	Prehnite	Chlorite
D3 - Strike-Slip	ORC-6-29-15-2	10	50	506574	5393382						
	ORC-7-9-15-4	21	51	509708	5388210	FI			x		
	ORC-7-9-15-6	21	52	509815	5388143						
	ORC-7-19-15-3	24	53	511074	5385640						
	ORC-7-23-15-2	31	54	510079	5384284	FI			x		x
	ORC-7-29-15-4	33	55	510123	5383852	XRD/FI		x	x		
	ORC-7-29-15-5	33	56	510123	5383852	XRD	x	x	x		
	ORC-7-29-15-6	33	57	510123	5383852	XRD		x	x		
	ORC-7-31-15-3	35	58	510101	5383606						
	ORC-8-1-15-2	36	59	509885	5387964						
	ORC-8-3-15-5	40	60	506045	5392036	XRD	x	x	x		
	ORC-9-1-15-1	42	61	509031	5388342						
	ORC-9-1-15-3	43	62	506584	5393370	XRD		x	x		
	ORC-9-1-15-4	43	63	506584	5393370	XRD	x	x	x		
D3 - Thrust	ORC-7-22-15-1	29	64	509920	5384494	XRD			x		
	ORC-8-2-15-3	39	65	506106	5392174	XRD		x	x		
	ORC-9-7-15-5	49	66	498378	5384062						
Garrison Schist	ORC-6-30-15-3	13	67	509054	5388289						
	ORC-6-30-15-4	13	68	509054	5388289						
	ORC-6-30-15-5	13	69	509054	5388289						
Crenulation	ORC-7-21-15-1	27	70	510855	5386085						
	ORC-7-31-15-2	35	71	510101	5383606						
	ORC-7-31-15-4	35	72	n/a	n/a						
	ORC-8-1-15-1	36	73	n/a	n/a						
	ORC-8-1-15-3	36	74	509890	5387956						
	ORC-8-1-15-5	37	75	510058	5387605						
	ORC-8-1-15-6	37	76	506078	5392006						
	ORC-9-2-15-1	45	77	501411	5384830						
	ORC-9-4-15-1	50	78	500665	5383450						

* Deformation event that sample was related to, samples of Garrison Schist, and samples suspected to have a crenulation cleavage.

** Field site numbers are shown in figures A1-A4 and include areas of structural observations.

Σ Sample map reference number is located in figures A5-A8 and represents the location within the field site where the samples were located.

ϕ North American 1983 coordinate system (zone 10N).

† Analysis used to test mineralogy and pressure-temperature conditions from samples. XRD - X-Ray Diffraction, FI - Fluid Inclusion. All samples were either made into a thick (~120μm) or thin (~25-35μm) sections and observed under a petrographic microscope.

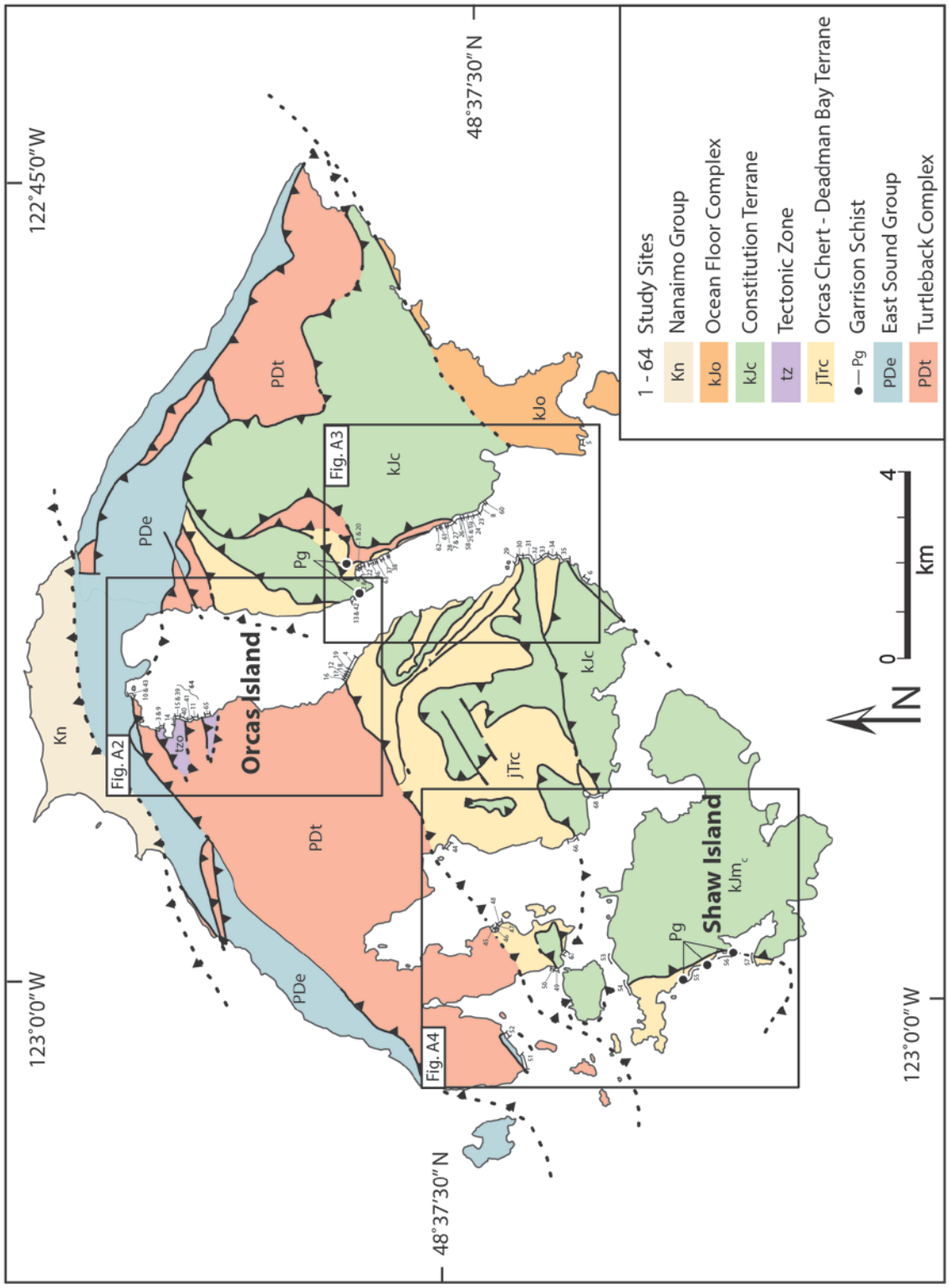

Figure A1. Geologic map of Orcas and Shaw Islands showing site locations referenced in figures 3, 5, and 11.

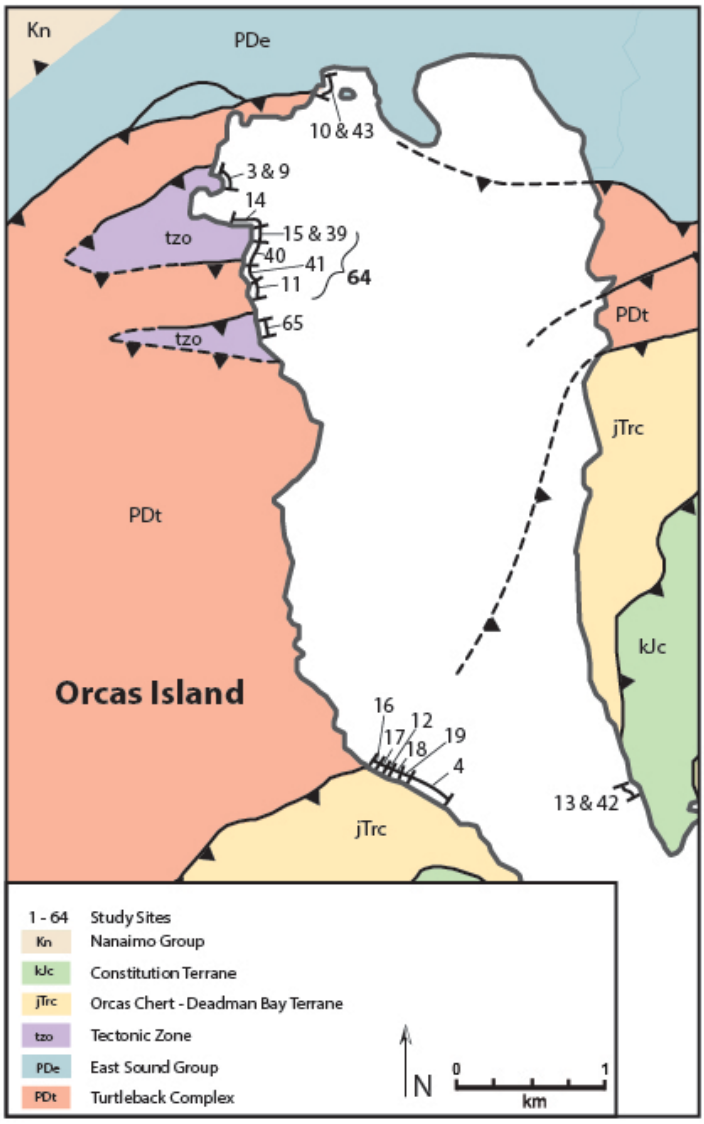

Figure A2. Inset map showing detailed site locations shown on figure A1.

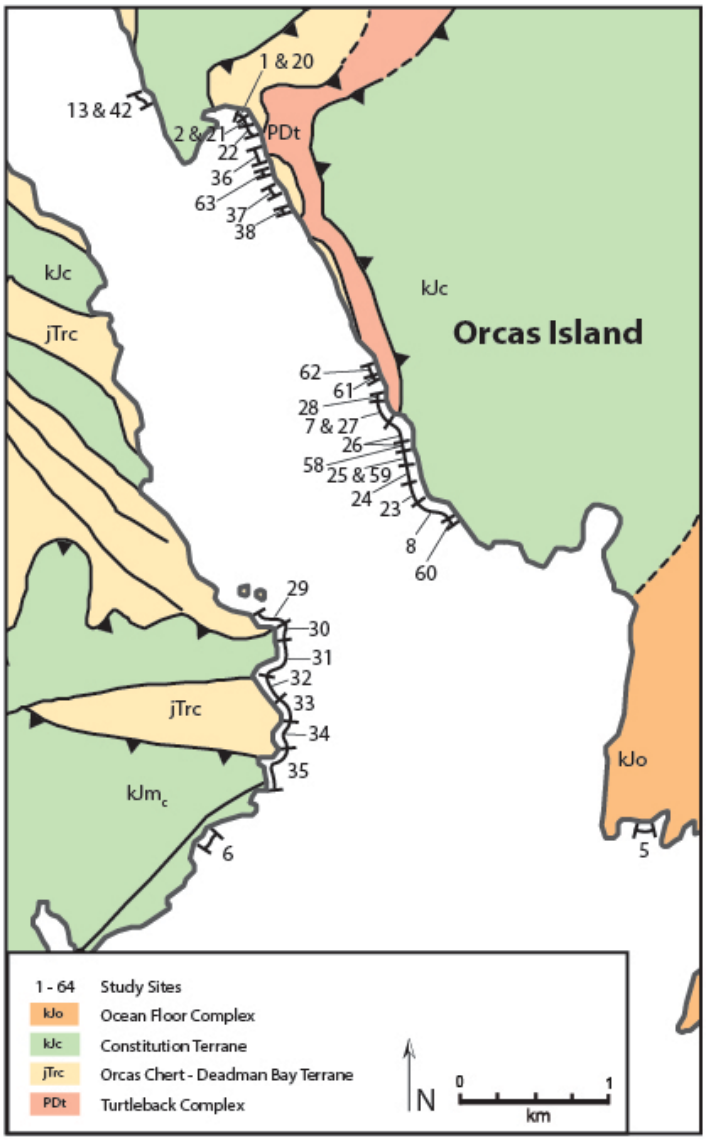

Figure A3. Inset map showing detailed site locations shown on figure A1.

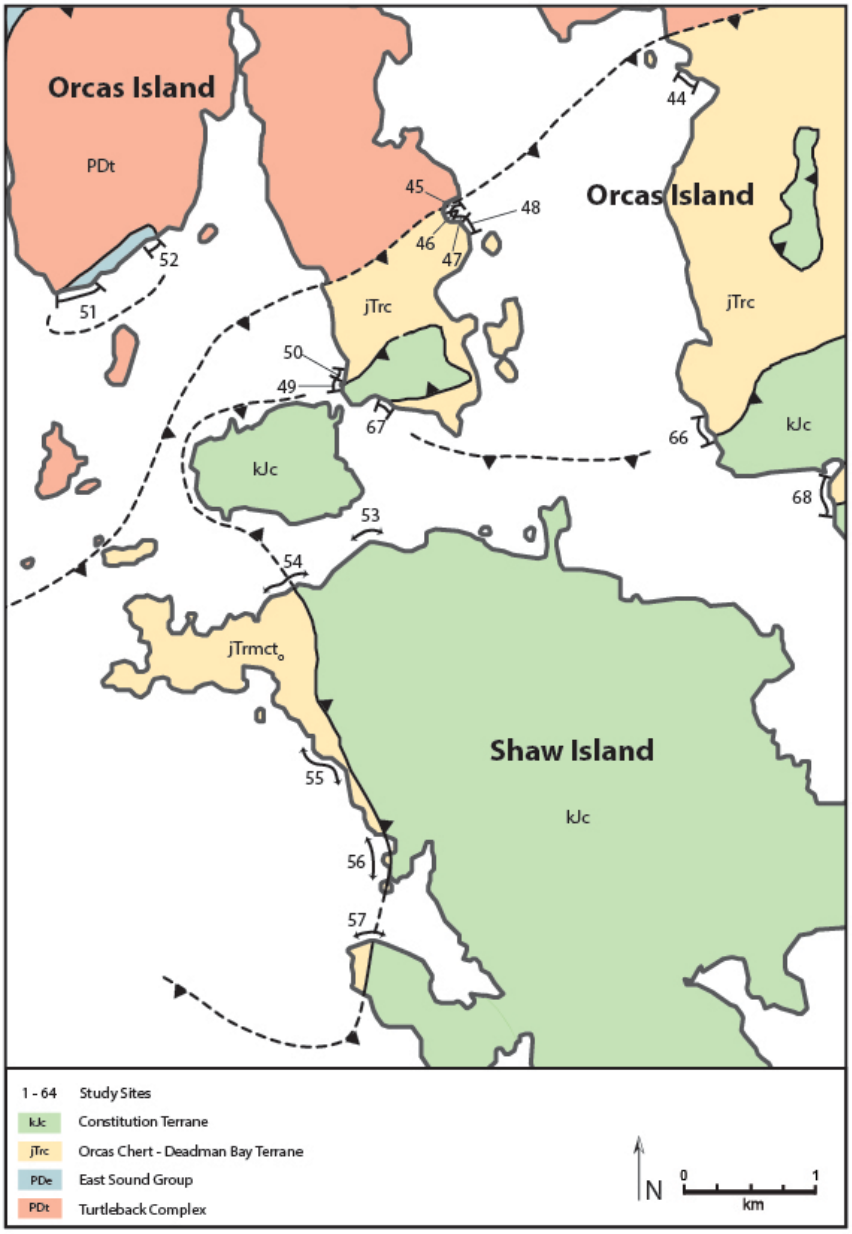

Figure A4. Inset map showing detailed site locations shown on figure A1.

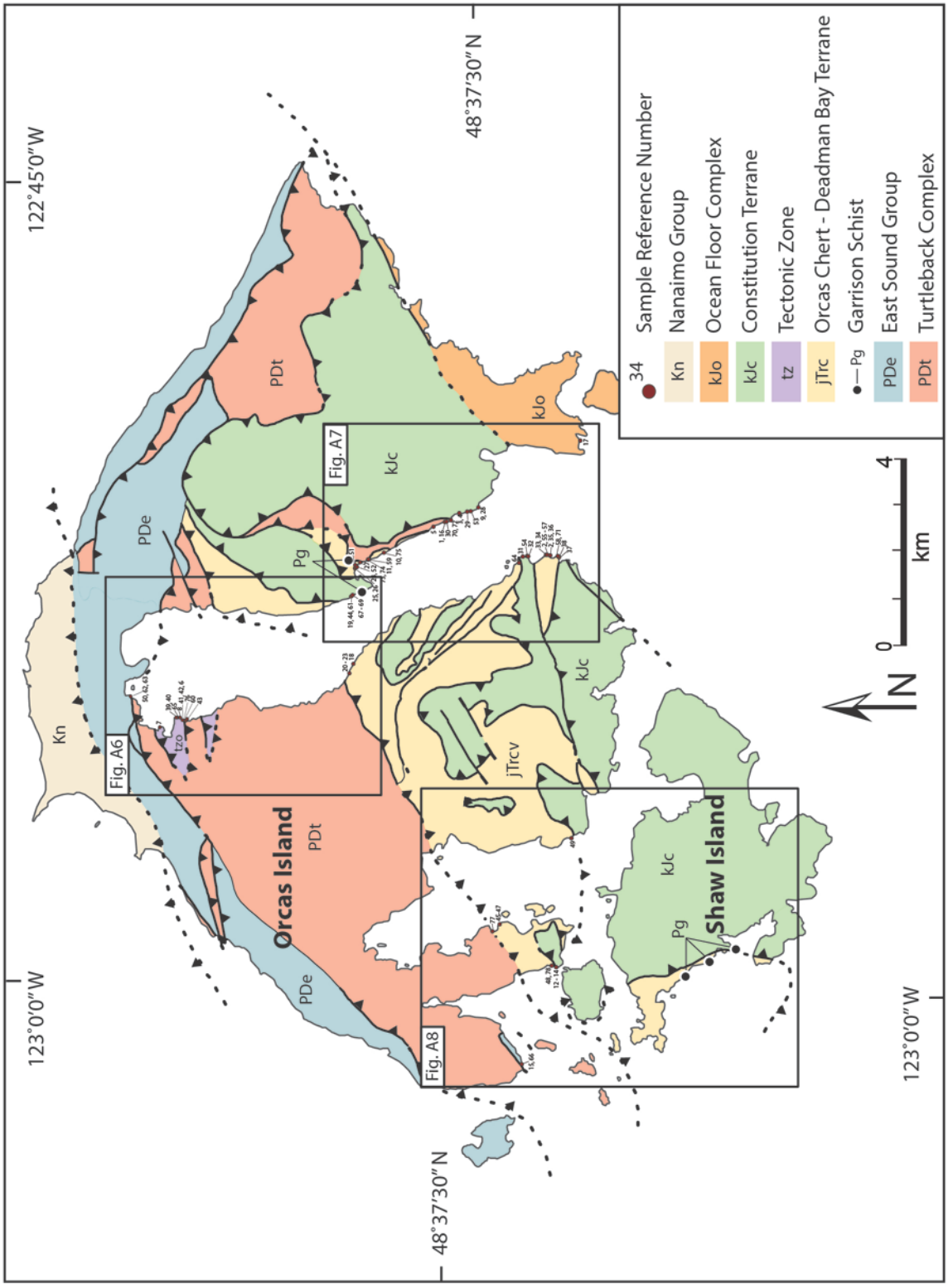

Figure A5. Geologic map of Orcas and Shaw Islands showing sample locations.

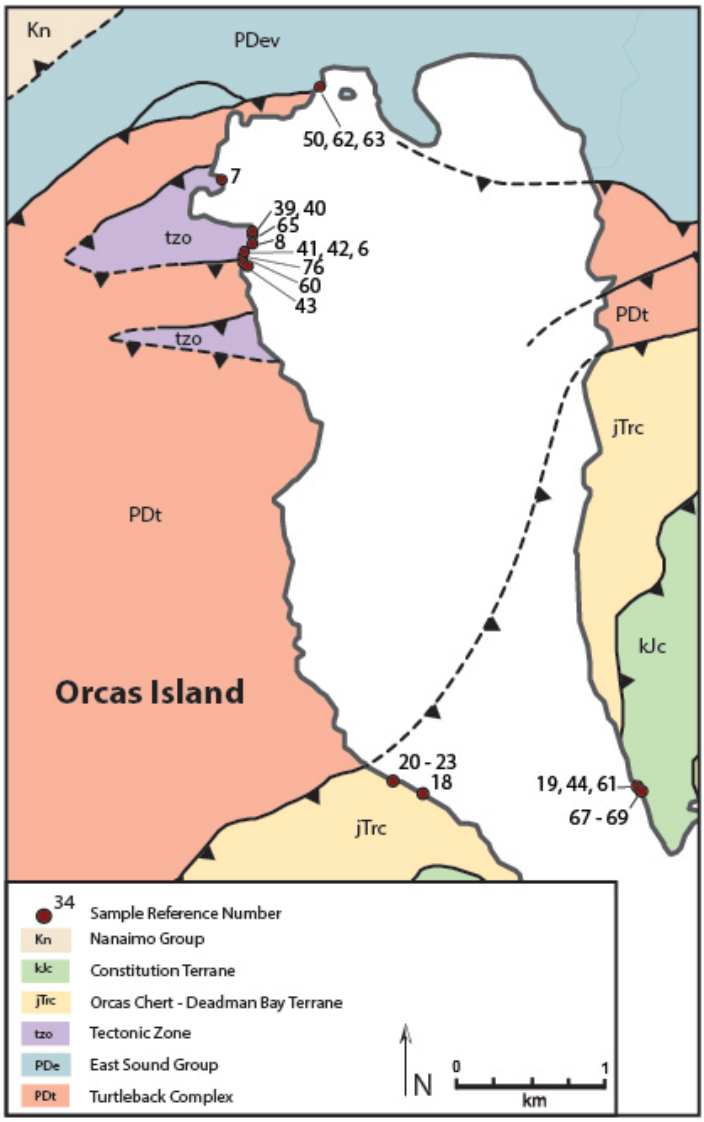

Figure A6. Inset map showing detailed sample locations shown on figure A5.

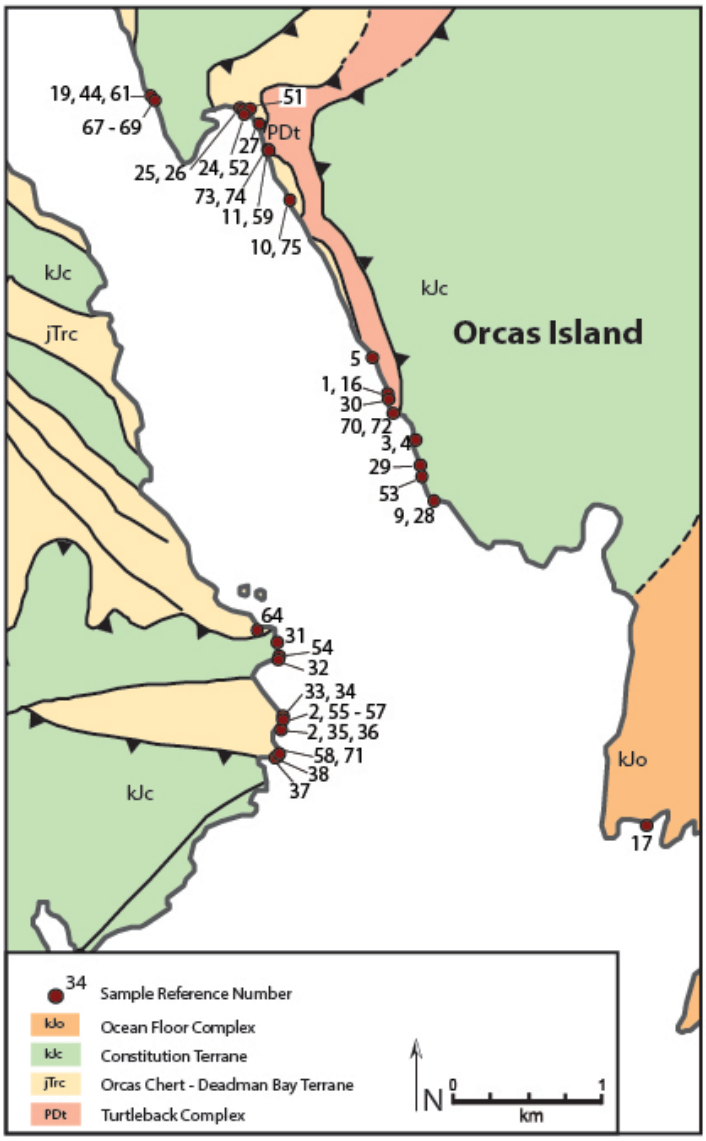

Figure A7. Inset map showing detailed sample locations shown on figure A5.

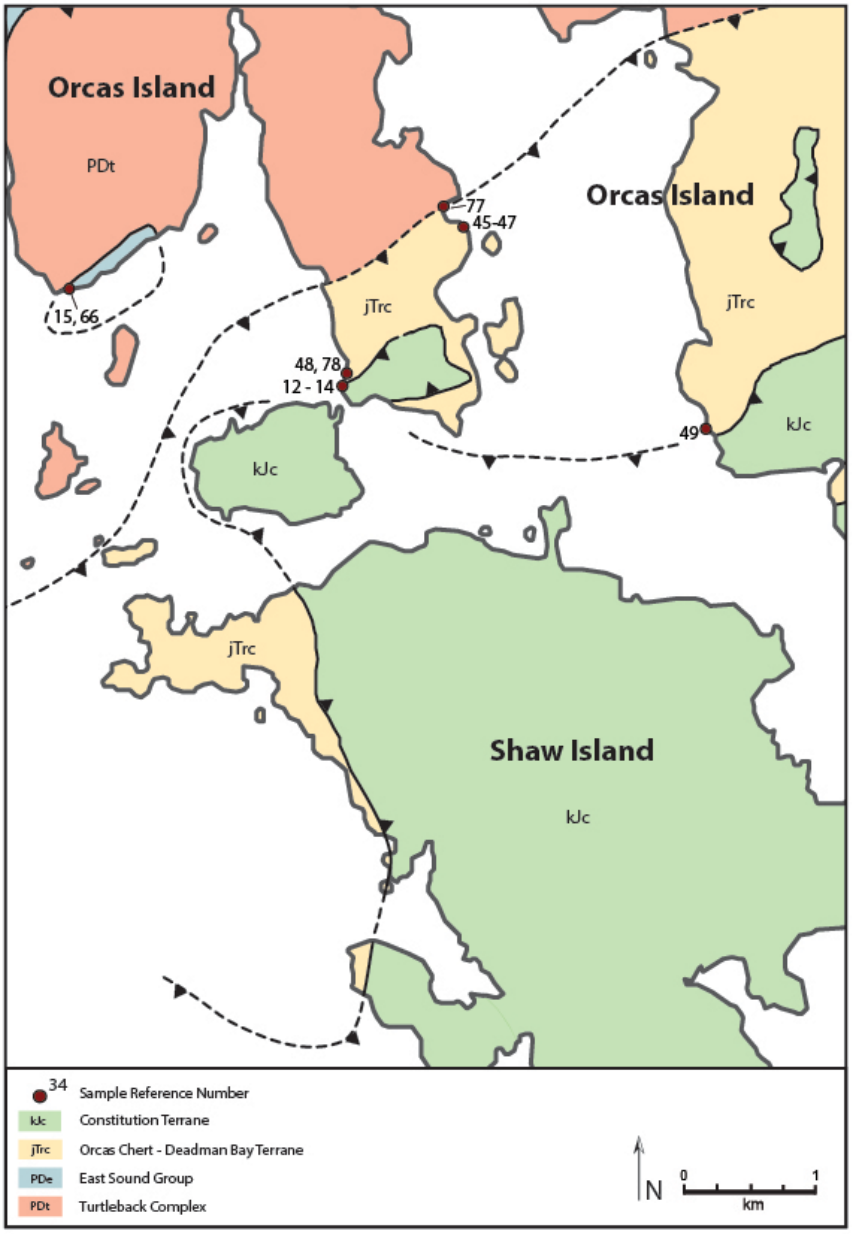

Figure A8. Inset map showing detailed sample locations shown on figure A5**.**